Charged pion form factor between Q^2=0.60 and 2.45 GeV^2. I. Measurements of the cross section for the ${}^{1}H(e,e'\pi^+)n$ reaction — **Source link** ↗

H. P. Blok, Tanja Horn, G. M. Huber, E. J. Beise ...+83 more authors

Related papers:

- Charged pion form factor between Q2=0.60 and 2.45 GeV2. II. Determination of, and results for, the pion form factor

- Determination of the Pion Charge Form Factor at Q 2 1:60 and 2:45 GeV=c 2

- Scaling study of the pion electroproduction cross sections

- Determination of the pion charge form factor for Q 2 = 0.60 1.60 GeV 2

- Measurement of the charged pion electromagnetic form factor.

Charged pion form factor between $Q^2 = 0.60$ and 2.45 GeV^2. I. Measurements of the cross section for the ^{1}H$(e, e'\pi^+)n$ reaction

H. P. Blok,[1,2] T. Horn,[3,4] G. M. Huber,[5] E. J. Beise,[3] D. Gaskell,[4] D. J. Mack,[4] V. Tadevosyan,[6] J. Volmer,[7,8] D. Abbott,[4] K. Aniol,[9] H. Anklin,[4,10] C. Armstrong,[11] J. Arrington,[12] K. Assamagan,[13] S. Avery,[13] O. K. Baker,[4,13] B. Barrett,[14] C. Bochna,[15] W. Boeglin,[10] E. J. Brash,[5] H. Breuer,[3] C. C. Chang,[3] N. Chant,[3] M. E. Christy,[13] J. Dunne,[4] T. Eden,[4,16] R. Ent,[4] H. Fenker,[4] E. Gibson,[17] R. Gilman,[4,18] K. Gustafsson,[3] W. Hinton,[13] R. J. Holt,[12] H. Jackson,[12] S. Jin,[19] M. K. Jones,[11] C. E. Keppel,[4,13] P. H. Kim,[19] W. Kim,[19] P. M. King,[3] A. Klein,[20] D. Koltenuk,[21] V. Kovaltchouk,[5] M. Liang,[4] J. Liu,[3] G. J. Lolos,[5] A. Lung,[4] D. J. Margaziotis,[9] P. Markowitz,[10] A. Matsumura,[22] D. McKee,[23] D. Meekins,[4] J. Mitchell,[4] T. Miyoshi,[22] H. Mkrtchyan,[6] B. Mueller,[12] G. Niculescu,[24] I. Niculescu,[24] Y. Okayasu,[22] L. Pentchev,[11] C. Perdrisat,[11] D. Pitz,[25] D. Potterveld,[12] V. Punjabi,[16] L. M. Qin,[20] P. Reimer,[12] J. Reinhold,[10] J. Roche,[4] P. G. Roos,[3] A. Sarty,[14] I. K. Shin,[19] G. R. Smith,[4] S. Stepanyan,[6] L. G. Tang,[4,13] V. Tvaskis,[7] R. L. J. van der Meer,[5] K. Vansyoc,[20] D. Van Westrum,[26] S. Vidakovic,[5] W. Vulcan,[4] G. Warren,[4] S. A. Wood,[4] C. Xu,[5] C. Yan,[4] W.-X. Zhao,[27] X. Zheng,[12] and B. Zihlmann[4,28]

(Jefferson Lab F_π Collaboration)

[1]*Dept. of Physics, VU university, NL-1081 HV Amsterdam, The Netherlands*
[2]*NIKHEF, Postbus 41882, NL-1009 DB Amsterdam, The Netherlands*
[3]*University of Maryland, College Park, Maryland 20742, USA*
[4]*Physics Division, TJNAF, Newport News, Virginia 23606, USA*
[5]*University of Regina, Regina, Saskatchewan S4S 0A2, Canada*
[6]*Yerevan Physics Institute, 375036 Yerevan, Armenia*
[7]*Faculteit Natuur- en Sterrenkunde, Vrije Universiteit, NL-1081 HV Amsterdam, The Netherlands*
[8]*DESY, Hamburg, Germany*
[9]*California State University Los Angeles, Los Angeles, California 90032, USA*
[10]*Florida International University, Miami, Florida 33119, USA*
[11]*College of William and Mary, Williamsburg, Virginia 23187, USA*
[12]*Argonne National Laboratory, Argonne, Illinois 60439, USA*
[13]*Hampton University, Hampton, Virginia 23668, USA*
[14]*Saint Mary's University, Halifax, Nova Scotia, Canada*
[15]*University of Illinois, Champaign, Illinois 61801, USA*
[16]*Norfolk State University, Norfolk, Virginia 23504, USA*
[17]*California State University, Sacramento, California 95819, USA*
[18]*Rutgers University, Piscataway, New Jersey 08855, USA*
[19]*Kyungpook National University, Taegu, Korea*
[20]*Old Dominion University, Norfolk, Virginia 23529, USA*
[21]*University of Pennsylvania, Philadelphia, Pennsylvania 19104, USA*
[22]*Tohoku University, Sendai, Japan*
[23]*New Mexico State University, Las Cruces, New Mexico 88003-8001, USA*
[24]*James Madison University, Harrisonburg, Virginia 22807, USA*
[25]*DAPNIA/SPhN, CEA/Saclay, F-91191 Gif-sur-Yvette, France*
[26]*University of Colorado, Boulder, Colorado 76543, USA*
[27]*M.I.T.–Laboratory for Nuclear Sciences and Department of Physics, Cambridge, Massachusetts 02139, USA*
[28]*University of Virginia, Charlottesville, Virginia 22901, USA*

Cross sections for the reaction ^{1}H$(e, e'\pi^+)n$ were measured in Hall C at Thomas Jefferson National Accelerator Facility (JLab) using the high-intensity Continuous Electron Beam Accelerator Facility (CEBAF) to determine the charged pion form factor. Data were taken for central four-momentum transfers ranging from $Q^2 = 0.60$ to 2.45 GeV^2 at an invariant mass of the virtual photon-nucleon system of $W = 1.95$ and 2.22 GeV. The measured cross sections were separated into the four structure functions σ_L, σ_T, σ_{LT}, and σ_{TT}. The various parts of the experimental setup and the analysis steps are described in detail, including the calibrations and systematic studies, which were needed to obtain high-precision results. The different types of systematic uncertainties are also discussed. The results for the separated cross sections as a function of the Mandelstam variable t at the different values of Q^2 are presented. Some global features of the data are discussed, and the data are compared with the results of some model calculations for the reaction ^{1}H$(e, e'\pi^+)n$.

045202-1

I. INTRODUCTION

A fundamental challenge in hadronic physics is trying to understand the structure of mesons and baryons in terms of their quark-gluon constituents, as given by the underlying theory of the strong interaction. This theory is known as quantum chromodynamics (QCD). Form factors of hadrons play an important role in this description, because they provide information about the internal structure of the hadron.

One of the simplest hadronic systems available for study is the pion, whose valence structure is a bound state of a quark and an antiquark. Its electromagnetic structure is parametrized by a single form factor $F_\pi(Q^2)$, which depends on $Q^2 = -q^2$, where q^2 is the four-momentum squared of the virtual photon. F_π is well determined up to Q^2 values of 0.28 GeV^2 by elastic π-e scattering [1–3], from which the charge radius has been extracted. Determining $F_\pi(Q^2)$ at larger values of Q^2 requires the use of pion electroproduction from a nucleon target. The longitudinal part of the cross section for pion electroproduction, σ_L, contains the pion exchange (t-pole) process, in which the virtual photon couples to a virtual pion inside the nucleon. This process is expected to dominate at small values of the Mandelstam variable $-t$, thus allowing for the determination of F_π.

Pion electroproduction data have previously been obtained for Q^2 values of 0.18–9.8 GeV^2 at the Cambridge Electron Accelerator (CEA) and at Cornell University [4,5], and at the Deutsches Elektronen-Synchrotron (DESY) [6,7]. Most of the high-Q^2 data have come from experiments at Cornell. In these experiments, F_π was extracted from the longitudinal cross sections, which were isolated by subtracting a model of the transverse contribution from the unseparated cross sections. Pion electroproduction data were also obtained at DESY [6–8] for Q^2 values of 0.35 and 0.7 GeV^2, and longitudinal (L) and transverse (T) cross sections were extracted using the Rosenbluth L/T separation method.

With the availability of the high-intensity, continuous electron beams and well-understood magnetic spectrometers at the Thomas Jefferson National Accelerator Facility (JLab) it became possible to determine L/T separated cross sections with high precision, and thus to study the pion form factor in the regime of $Q^2 = 0.5$–3.0 GeV^2. In 1997, high-precision pion electroproduction data for Q^2 values between 0.60 and 1.60 GeV^2 were acquired at JLab at a value of the invariant mass of the photon-nucleon system of $W = 1.95$ GeV. The main results were published in Ref. [9], with an updated analysis of these data published in Ref. [10]. In 2003, the range $Q^2 = 1.60$–2.45 GeV^2 was studied at $W = 2.22$ GeV [11]. At each Q^2 value, cross sections were obtained at two different values of the virtual photon polarization, ϵ, allowing for the separation of the longitudinal and transverse components of the cross section.

The purpose of this work is to describe the experiment and analysis in detail and to present and discuss additional results. The discussion has been split into two parts. This paper describes the experiment and analysis, presents the measured cross sections, including the separation into the structure functions, along with a detailed discussion of the systematic uncertainties, and compares them with previous L/T separated data and with theoretical calculations for the

cross section. The paper immediately following [12] discusses the determination of F_π and presents the resulting F_π values, including all uncertainties. These values are then compared with various theoretical predictions. This division was chosen to separate the determination of the cross section, with its various experimental issues, from the extraction of F_π from the measured cross sections, which is model dependent. If more advanced or other models will become available, new values for F_π may be extracted from the same cross sections.

This paper is organized as follows. In the next section, the basic formalism of the ^{1}H($e, e'\pi^+$)n reaction is presented. In Sec. III, the experiment performed at JLab is described, including the experimental setup and spectrometer calibrations. The data analysis and a discussion of the various efficiencies that play a role are presented in Sec. IV. The determination of the unseparated cross sections and the separation of these cross sections into the four different structure functions is described in Sec. V. The results are presented in Sec. VI. The global features of the separated cross sections are discussed, and a comparison is made with the results of theoretical calculations. In this discussion, the data from Refs. [6–8] are also included. The paper concludes with a short summary.

II. GENERAL FORMALISM FOR EXCLUSIVE PION ELECTROPRODUCTION

A. Kinematics

The kinematics of the ^{1}H($e, e'\pi^+$)n reaction are displayed in Fig. 1. The three-momentum vectors of the incoming and scattered electrons are denoted by **k** and **k**′, respectively. Together they define the scattering plane. The corresponding four-momenta are $k \equiv (E, \mathbf{k})$ and $k' \equiv (E', \mathbf{k}')$. The electron scattering angle is denoted by θ_e. The four-momentum of the transferred virtual photon, $q \equiv (\omega, \mathbf{q})$, is given by $q \equiv k - k'$. As usual, the variable Q^2 is defined as the negative of the transferred four-momentum squared: $Q^2 \equiv -q^2$. The three-momentum **q** and the three-momentum vector of the pion $\mathbf{p}_\pi$ together define the reaction plane. The angle between the scattering plane and the reaction plane is denoted by ϕ_π, while the angle (in the laboratory system) between $\mathbf{p}_\pi$ and **q** is θ_π.

The missing energy and missing momentum are defined as

$$E_m = E_e - E_{e'} - E_\pi, \tag{1}$$
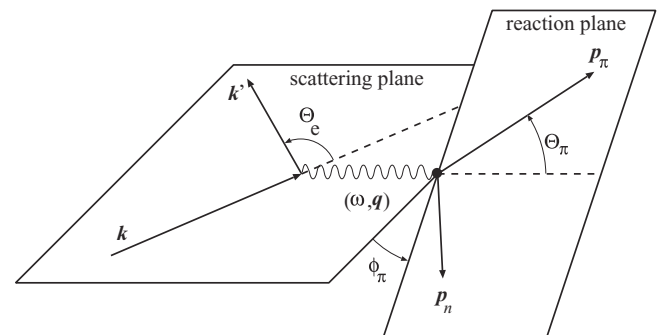
$$\mathbf{p}_m = \mathbf{q} - \mathbf{p}_\pi. \tag{2}$$

FIG. 1. Kinematics of the ^{1}H($e, e'\pi^+$)n reaction in the laboratory frame.

The missing mass of the recoil system can then be expressed as $M_m = \sqrt{E_m^2 - \mathbf{p^2}_m}$. In the case of the reaction $^1\mathrm{H}(e, e'\pi^+)n$, the missing mass is given by the neutron mass $M_m = m_n$.

The $^1\mathrm{H}(e, e'\pi^+)n$ reaction can conveniently be described using three Lorentz invariants. In addition to Q^2, we use the invariant mass of the virtual photon-nucleon system W (which can be expressed as $W = \sqrt{M_p^2 + 2M_p\omega - Q^2}$, where M_p is the proton mass) and the Mandelstam variable $t = (p_\pi - q)^2$. The latter can be expanded into

$$t = (E_\pi - \omega)^2 - |\mathbf{p}_\pi|^2 - |\mathbf{q}|^2 + 2\,|\mathbf{p}_\pi|\,|\mathbf{q}|\cos\theta_\pi. \quad (3)$$

In the $^1\mathrm{H}(e, e'\pi^+)n$ reaction, t is always negative. The minimum value $-t_{\min}$ of $-t$ is reached for $\theta_\pi = 0$. The minimum value of $-t$ increases for increasing values of Q^2 and decreasing values of W.

B. Cross sections

Describing the incoming and outgoing electrons by plane waves, the cross section for the $^1\mathrm{H}(e, e'\pi^+)n$ reaction can be written in the one-photon exchange approximation as

$$\frac{d^5\sigma}{dE'\,d\Omega_{e'}\,d\Omega_\pi} = \Gamma_V \frac{d^2\sigma}{d\Omega_\pi}. \quad (4)$$

Here Γ_V is the virtual photon flux factor

$$\Gamma_v = \frac{\alpha}{2\pi^2}\frac{E'}{E}\frac{K}{Q^2}\frac{1}{1-\epsilon}, \quad (5)$$

where α is the fine structure constant, the factor $K = (W^2 - M_p^2)/(2M_p)$ is the equivalent real-photon energy, which is the laboratory energy a real photon would need to produce a system with invariant mass W, and

$$\epsilon = \left(1 + \frac{2|\mathbf{q}|^2}{Q^2}\tan^2\frac{\theta_e}{2}\right)^{-1} \quad (6)$$

is the polarization of the virtual photon. The two-fold differential cross section can be written in terms of an invariant cross section as

$$\frac{d^2\sigma}{d\Omega_\pi} = J\frac{d^2\sigma}{dt\,d\phi}, \quad (7)$$

where J is the Jacobian for the transformation from Ω_π to t, ϕ.

The cross section can be decomposed into four structure functions corresponding to the polarization states of the virtual photon: a longitudinal one (L), a transverse one (T), and two interference terms (LT and TT) [13]:

$$2\pi\frac{d^2\sigma}{dtd\phi} = \epsilon\frac{d\sigma_{\mathrm{L}}}{dt} + \frac{d\sigma_{\mathrm{T}}}{dt} + \sqrt{2\epsilon(\epsilon+1)}\frac{d\sigma_{\mathrm{LT}}}{dt}\cos\phi$$
$$+\epsilon\frac{d\sigma_{\mathrm{TT}}}{dt}\cos 2\phi, \quad (8)$$

where the $d\sigma_X/dt$ depend on Q^2, W, and t. The dependence of the interference structure functions on θ_π features the following leading-order behavior [14]: $d\sigma_{\mathrm{LT}}/dt \sim \sin\theta_\pi$ and $d\sigma_{\mathrm{TT}}/dt \sim \sin^2\theta_\pi$. Therefore the interference structure functions are zero in parallel kinematics ($\theta_\pi = 0$), i.e., at $t_{\min}$.

The four structure functions can be isolated if data are taken at different values of ϵ and ϕ_π, while W, Q^2, and t are kept constant. The photon polarization ϵ can be varied by changing the electron energy and scattering angle (the so-called Rosenbluth or L/T separation). The angle ϕ_π can be varied by measuring the pion left and right of the $\mathbf{q}$ vector, and out of the scattering plane.

III. EXPERIMENT AND SETUP

The two F_π experiments were carried out in 1997 (Fpi-1 [15]) and 2003 (Fpi-2 [16]) in Hall C at JLab. The unpolarized electron beam from the Continuous Electron Beam Accelerator Facility (CEBAF) was incident on a liquid hydrogen target. Two moderate acceptance, magnetic focusing spectrometers were used to detect the particles of interest. The produced charged pions were detected in the high momentum spectrometer (HMS), while the scattered electrons were detected in the short orbit spectrometer (SOS).

A. Experiment kinematics

The choice of kinematics for the two experiments was based on maximizing the range in Q^2 for a value of the invariant mass W above the resonance region. For each Q^2, data were taken at two values of the virtual photon polarization ϵ, with $\Delta\epsilon$ typically >0.25. This allowed for a separation of the longitudinal, transverse, LT, and TT cross sections.

Constraints on the kinematics were imposed by the maximum available electron energy, the maximum central momentum of the SOS, and the minimum HMS angle. The central kinematics for the two experiments are given in Table I. In parallel kinematics, i.e., when the pion spectrometer is situated in the direction of the $\mathbf{q}$ vector, the acceptances of the two spectrometers do not provide a uniform coverage in ϕ_π. Thus, to attain full coverage in ϕ_π, additional data were taken with the HMS at a slightly smaller and a larger angle than the central angle for the high ϵ settings. At low ϵ, only the larger angle setting was possible.

B. Accelerator

The experiments made use of the unpolarized, continuous wave (CW, 100% duty factor) electron beam provided by the JLab accelerator [17,18]. The beam has a microstructure that helps in the identification of coincident events, which is further described in Sec. IV. Beam currents were between 10 and 100 μA.

To precisely determine the kinematics, the beam position and angle on target were monitored using beam position monitors (BPMs). The accuracy of the position measurement was about 0.5 mm and about 0.2 mrad for the incident angle. In the Fpi experiments, the beam current was measured by two beam current monitors (BCM1 and BCM2). To minimize drifts in the gain, both BCMs are calibrated to an absolute reference. The calibration is performed using an Unser current monitor [19], which has an extremely stable gain but suffers

TABLE I. Central kinematic settings used in the experiments. In addition, settings were taken with the pion arm (HMS) at smaller and larger angles ($\theta_\pi = \theta_q \pm 4°$ in Fpi-1 and $\theta_\pi = \pm 3°$ in Fpi-2) for the high-ϵ settings and at the larger angle only for the low-ϵ data. The scattered electron was always detected in the SOS.

Q^2 (GeV^2)	W (GeV)	$|t|_{min}$ (GeV^2)	E (GeV)	θ_e (GeV)	E' (GeV)	θ_π (GeV)	P_π (GeV)	ϵ
				Fpi-1 settings				
0.60	1.95	0.030	2.445	38.40	0.567	9.99[a]	1.856	0.37
0.60	1.95	0.030	3.548	18.31	1.670	14.97	1.856	0.74
0.75	1.95	0.044	2.673	36.50	0.715	11.46	1.929	0.43
0.75	1.95	0.044	3.548	21.01	1.590	15.45	1.929	0.70
1.00	1.95	0.071	2.673	47.26	0.582	10.63	2.048	0.33
1.00	1.95	0.071	3.548	25.41	1.457	15.65	2.048	0.65
1.60	1.95	0.150	3.005	56.49	0.594	10.49	2.326	0.27
1.60	1.95	0.150	4.045	28.48	1.634	16.63	2.326	0.63
				Fpi-2 settings				
1.60	2.22	0.093	3.779	43.10	0.786	9.53[b]	2.931	0.33
1.60	2.22	0.093	4.709	43.10	1.650	12.54	2.931	0.58
2.45	2.22	0.189	4.210	51.48	0.771	9.19[c]	3.336	0.27
2.45	2.22	0.189	5.246	29.43	1.740	12.20	3.336	0.54

[a]Here, the value of θ_π denotes the angle of the momentum transfer θ_q. The actual HMS angle was 10.49°.
[b]The actual HMS angle was 10.50°.
[c]The actual HMS angle was 10.54°.

from large drifts in the offset on short time scales. The run-to-run uncertainty in the current as measured by BCM1 and BCM2 was found to be about 0.2% at 100 μA. Adding the normalization uncertainty from the Unser monitor, which is estimated to be 0.4%, results in an absolute uncertainty for the charge measurement of 0.5%. A more detailed description of the beam current monitors can be found in Ref. [20].

To reduce local density reductions of the liquid targets, the beam was rastered using a pair of fast raster magnets to a 1.2×1.2 mm^2 pattern during Fpi-1 and to a 2×2 mm^2 profile during Fpi-2. The raster position was recorded event by event. A more detailed description of the fast raster system can be found in Ref. [21].

The energy of the electron beam in Hall C is measured using the deflection of the electron beam in a known magnetic field in the Hall C arc. Including the uncertainty in the field integral and the angular uncertainty, the beam energy can be determined with a precision of $\frac{\delta p}{p} \approx 5 \times 10^{-4}$. A detailed description of the beam energy measurement using the arc method is available in Ref. [22].

C. Target

Both Fpi experiments used a three-loop cryogenic target stack, mounted together with a special optics target assembly. The cryogenic targets use the same coolant supply and are cooled on the cryotarget ladder simultaneously. Two different cryogenic target cell types were used. In the Fpi-1 experiment, a 4.5 cm long cylindrical cell with the axis mounted horizontally and parallel to the beam direction was used (horizontal-flow "beer can" design). In the Fpi-2 experiment, a 4.0 cm diameter cylindrical cell with vertical axis (vertical-flow "tuna can" design) was used. The cell walls are made from aluminum alloy T6061 with a thickness of

0.0127 cm (the beer can front wall is half as thick). The cryogenic targets are typically kept at a nominal operating temperature about 2 K below the boiling point. The hydrogen target was kept at a temperature of 19 K, giving a density of 0.0723 ± 0.0005 g/cm^3 [23]. Cell temperatures were kept constant to within 100 mK during the experiment. Since the uncertainty in temperature gives a negligible contribution, the uncertainty in the target density is completely due to the equation of state.

The optics target assembly was mounted beneath the cryogenic target ladder. It consists of five carbon foils (the "quintar") and two aluminum foils. A schematic design of the quintar is shown in Fig. 2. By moving the target stack vertically, the five targets can be moved into the beam individually or simultaneously. The solid carbon foils are used with the beam incident on two or five (quintar) foils simultaneously for the purpose of calibrating the vertex position z along the beam direction (see Sec. IV C). During Fpi-1, the quintar z positions (relative to the nominal target center) were $z = \pm 6.0, \pm 3.0,$ and 0 cm; while in Fpi-2, they were $z = \pm 7.5, \pm 3.8,$ and 0 cm. The two aluminum foils situated at $z = \pm 2.25$ cm (Fpi-1) or $z = \pm 2.0$ cm (Fpi-2) constitute the "dummy target" used to measure the contribution of the aluminum cell wall to the cryotarget yields. The material of the aluminum dummy targets is Al-T7075 ($\rho = 2.795$ g/cm^2), a higher strength alloy. The dummy target foils are approximately seven times thicker than the cryotarget cell walls. Further details on the mechanical aspects of the cryotargets can be found in Refs. [23–25].

D. Spectrometers

A schematic overhead view of the Hall C spectrometers is shown in Fig. 3. Both spectrometers have a relatively large momentum and solid angle acceptance and are equipped with
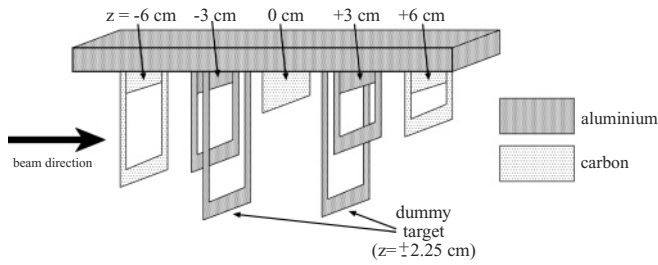
FIG. 2. Schematic view of the quintar optics target assembly (not to scale).

similar and highly versatile detector packages. The short orbit spectrometer (SOS), which was optimized for the detection of short-lived particles, has a relatively short flight path of about 7.4 m and a maximum central momentum of 1.74 GeV/c. The high momentum spectrometer (HMS) has a 26 m path length and a maximum central momentum of 7.5 GeV/c.

1. High momentum spectrometer

The HMS consists of three superconducting quadrupole magnets and a 25° vertical-bend dipole magnet used in a point-to-point tune for the central ray. The momentum acceptance of the HMS is about ±10%. All magnets are mounted on a common carriage, which can be moved on rails around a rigidly mounted central bearing. A detailed description of
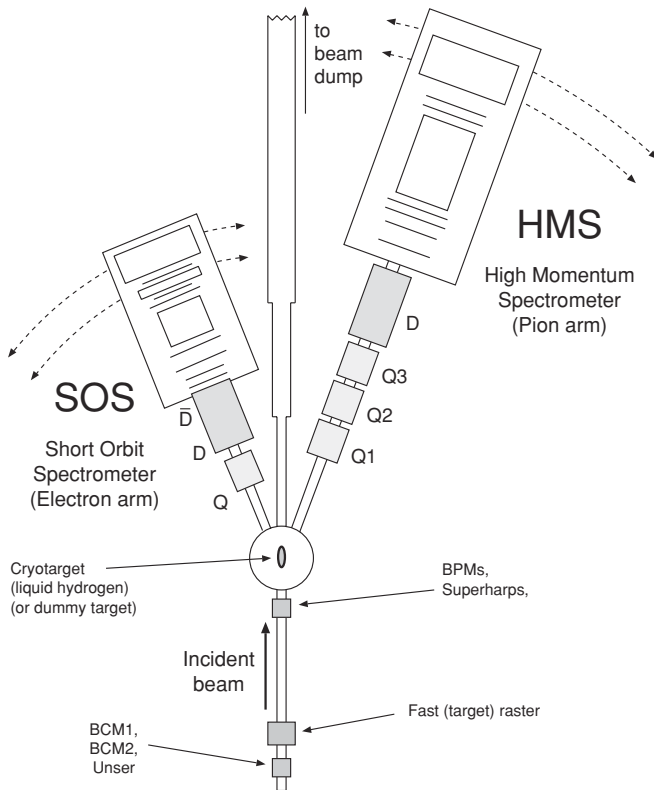
TABLE II. Nominal specifications for the HMS and SOS.

Quantity	HMS	SOS
Max. central mom.	7.5 GeV/c	1.74 GeV/c
Optical length	26.0 m	7.4 m
Angular range	10.5°–85°	13.4°–165°
Momentum acceptance	±10%	±20%
Momentum resolution	<0.1%	0.1%
Solid angle[a]	6.7 msr	7.5 msr
In-plane ang. acc.[a]	±27.5 mrad	±57.5 mrad
Out-of-plane ang. acc.[a]	±70 mrad	±37.5 mrad
In-plane ang. res.	1.0 mrad	2.5 mrad
Out-of-plane ang. res.	2.0 mrad	0.5 mrad
Extended target acc.	±7 cm	±1.5 cm
Vertex recon. accuracy	2 mm	1 mm

[a]The solid angle and angular acceptances are given for the large collimators in both the HMS and SOS.

the spectrometer hardware is given in Ref. [26]. The design specifications are given in Table II.

The HMS detector stack shown in Fig. 4 is situated in a concrete shielding hut 26 m from the spectrometer pivot. To minimize multiple scattering and to provide thermal insulation, the region between the first quadrupole (Q1) and the entrance to the shielding hut is evacuated. The vacuum region is separated from the surrounding environment by vacuum windows. During Fpi-1, a Mylar spectrometer exit window was used; this window was replaced with a 0.508 mm titanium window (radiation length of 3.56 cm) prior to the Fpi-2 experiment. A detailed discussion of the Hall C spectrometer vacuum system and vacuum windows can be found in Ref. [26].

The angular acceptance of the HMS is defined by a collimator positioned in a collimator box between the target and the first quadrupole magnet. The collimator box contains two octagonal collimators ("large" and "small"), a sieve slit, which is exclusively used for optics calibration (see Sec. IV C), and an empty position. The large collimator, which was used in the experiments, gives a solid angle of 6.8 msr. The collimators are made from 3.175 cm thick HEAVYMET, which is a machinable tungsten alloy with 10% CuNi. The large and small collimators are flared along the inside edge to match the particle distribution emanating from the target, but the holes in the sieve slit collimator are not. The front face of the collimator is at a distance of 166.4 cm from the center of the target. A vacuum extension ("snout") in front of the collimator box limits the amount of air traversed between the target chamber vacuum and the vacuum inside the HMS to 15 cm. With this configuration, the minimum central angle is about 10.5°.

To set the HMS momentum in a reproducible fashion, the dipole is set by field using an NMR probe in the magnet, with a reproducibility of the magnetic field at the level of one part in 10^4 and a stability to within one part in 10^5. The quadrupoles are set by current using a special procedure to ensure reproducibility [27] and are monitored using the power supply readback current and Hall probes.

In 1998, the Hall probes indicated a relatively large current offset in the third quadrupole, which was addressed through a

FIG. 3. Schematic view of the Hall C spectrometers with the target and beamline.
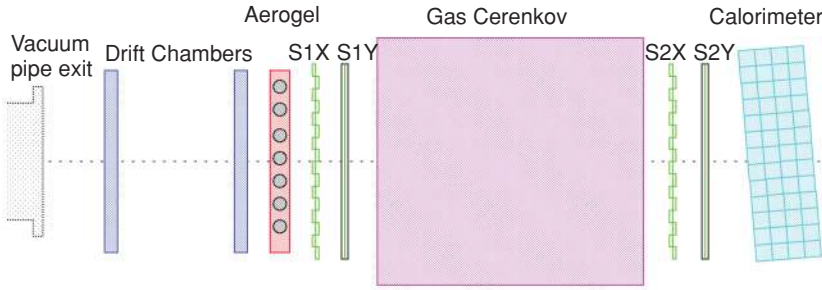
FIG. 4. (Color online) Schematic side view of the HMS detectors during Fpi-2. The lead-glass calorimeter is tilted 5° relative to the central ray to minimize the loss of particles in the spaces between the calorimeter blocks.

correction to the magnet field setting routine [28]. During the Fpi-2 experiment, it was found that a small offset in the third quadrupole (Q3) set current persisted. This residual Q3 offset was addressed by an ad-hoc correction to the reconstruction of all data, as will be described further in Sec. IV D. In practice, its influence on the optical properties in the extraction of the final result is negligible.

2. Short orbit spectrometer

The SOS spectrometer, which has a $\overline{QDD}$ configuration, is a copy of the medium resolution spectrometer at the Los Alamos Meson Physics Facility (LAMPF) [29]. The three magnets are nonsuperconducting and water cooled and rest on a common carriage. The quadrupole focuses in the nondispersive direction, the first dipole bends particles with the central momentum upward by 33°, and the second one bends them downward by 15°. In addition to the quadrupole magnet, the fringe fields arising from the curved shape of the pole tips of the dipole magnets provide focusing. A collimator box similar to the one discussed above for the HMS is attached to the front of the quadrupole. The specifications of the SOS are given in Table II.

The SOS magnets are set by field, measured with Hall probes, providing a short-term reproducibility of ± 1.5 G, with long-term drifts of a few parts in 10^4. To ensure that the magnetic fields always lie on the same hysteresis curve, a particular cycling procedure was used. At the highest momenta, a correction to the central momentum was applied to account for saturation effects from the iron in the magnets (see Sec. IV C).

E. Detector packages

The detector packages in the HMS and SOS are similar and consist of two horizontal drift chambers for track reconstruction, four scintillator hodoscope arrays used for triggering and time-of-flight measurements, and a threshold gas Cherenkov detector and lead-glass calorimeter for particle identification (mainly pion-electron separation). A schematic view of the HMS detector package is shown in Fig. 4. For the Fpi-2 experiment, an aerogel Cherenkov detector (shown in Fig. 4) was added to the HMS detector package to enhance the pion-proton separation at higher momenta. The individual detector components and their significance for data analysis are described in the following sections. A complete review

of the detector packages, including the detailed geometry and performance evaluation, can be found in Refs. [20,24,26,30].

1. Drift chambers

Both spectrometers are equipped with a pair of drift chambers. Each drift chamber contains six planes of sense wires with a spacing of 1 cm. The wires are oriented in three (SOS) or four (HMS) different directions to allow the measurement of the x and y hit positions of an incident charged particle. The redundancy in number of planes helps to resolve the ambiguity of multiple hits, to determine on which side of a wire a particle has passed ("left-right ambiguity"), and to determine a single-chamber estimate of the particle trajectory.

A detailed description of the HMS drift chambers can be found in Ref. [31]. The wire planes are ordered x, y, u, v, y', x'. The x and y planes measure the vertical and horizontal track position, respectively. The u and v plane wires are rotated by $\pm 15°$ with respect to the x wires. This small angle makes the u and v planes x-like, with the effect that the redundancy in the x direction is good, but poor in the y direction. The position resolution for the HMS drift chambers is typically 150 μm per plane. The two drift chambers are placed at distances of 40 cm before and after the HMS nominal focal plane.

The planes in the SOS drift chambers are ordered u, u', x, x', v, v'. There are no explicit y planes, but the u and v wire planes are rotated by $\pm 60°$ with respect to the x wires. As a result, the y resolution of the SOS detector is better than in the HMS. Unlike in the HMS, the wire planes form pairs with the sense wires offset by half a cell spacing (0.5 cm). That means that the left-right ambiguity is resolved if both planes of a pair are hit. The position resolution of the SOS drift chambers is approximately 200 μm per plane. The two drift chambers are placed ≈ 25 cm before and after the nominal focal plane of the SOS.

2. Hodoscopes

Hodoscopes consisting of two scintillator planes are located before and after the gas Cherenkov counters in both spectrometers. In the HMS, the first plane of each hodoscope is segmented into "paddles" in the vertical, the second one in the horizontal direction. In the SOS, the order is reversed. The hodoscopes serve two purposes: triggering of the data acquisition system, and measuring the particle velocity using

the time-of-flight between the two hodoscope planes. Each of the scintillator paddles in the HMS hodoscopes has a thickness of 1.0 cm and a width of 8 cm, with an overlap of 0.5 cm, while those in the SOS have thickness 1.0 cm, width 7.5 cm, and an overlap of 0.5 cm. Each scintillator paddle is read out by phototubes at both ends. The signals of all photomultipliers on each side of the plane are OR-ed and the signals from the two sides then are AND-ed to form the signals **S1X**, **S1Y**, **S2X**, and **S2Y**. The signal **S1(S2)** is the OR of **S1X** with **S1Y(S2X** with **S2Y)**. The role of the hodoscope signals in the trigger system is discussed in Sec. III F.

3. Gas Cherenkov detectors

The HMS Cherenkov detector is a cylindrical tank with two parabolic mirrors at the end and two photomultiplier tubes inside, mounted on the top and bottom surfaces. The gas Cherenkov was filled with C_4F_{10} gas at 79 kPa (Fpi-1) or 47 kPa (Fpi-2). The index of refraction at these pressures is 1.0011 (Fpi-1) and 1.00066 (Fpi-2), giving electron thresholds below 10 MeV/c and pion thresholds of 3.0 (Fpi-1) or 3.8 (Fpi-2) GeV/c. The SOS Cherenkov detector has four mirrors and four phototubes. The detector is maintained at atmospheric pressure with Freon-12 (CCl_2F_2), with a refractive index of 1.00108, yielding a pion threshold of 3 GeV/c, well above the maximum momentum setting of the SOS. A more detailed description of the Cherenkov detectors can be found in Ref. [30].

4. Lead-glass calorimeter

Each lead-glass calorimeter uses $10 \times 10 \times 70$ cm^3 blocks arranged in four planes and stacked 13 and 11 blocks high in HMS and SOS, respectively. The entire detector is tilted by 5° relative to the central ray of the spectrometer to minimize losses due to particles passing through the gaps between the blocks. More detailed information about the calorimeter system hardware can be found in Ref. [26].

5. HMS aerogel Cherenkov detector

Above momenta of 3 GeV/c, separation of pions and protons in the HMS by measuring the particle velocity with the scintillators of the hodoscopes is not possible in view of the required time-of-flight resolution. Therefore, an aerogel threshold Cherenkov detector was added to the HMS detector package in 2003. Aerogel with a refractive index of $n = 1.030$ was used as the medium, giving a pion threshold of 0.57 GeV/c and a proton threshold of 3.8 GeV/c, allowing rejection of protons up to the highest HMS momentum setting used in Fpi-2 of 3.336 GeV/c. Further details on the design and testing of the HMS aerogel Cherenkov detector can be found in Ref. [32].

F. Trigger system and data acquisition

To keep the event rate below the current limit of the data acquisition system ($\approx$3 kHz), events of interest are selected by the formation of a combination of logic signals that indicate when a particular set of detectors fired. This combination is used to decide if the event should be recorded, i.e., a pretrigger should be formed.

Both spectrometers have a single-arm trigger logic system, which can be subdivided into two components, one coming from the hodoscopes, and one from the combination of signals from the gas Cherenkov and the calorimeter. The most basic trigger is the **SCIN** trigger from the hodoscopes, which is satisfied if there is a hit in three out of the four planes. Figure 5 shows a schematic of the single-arm trigger used.

The main component of the standard electron trigger, **ELREAL**, is the scintillator information, which is provided by two signals (**STOF**, which requires the AND of **S1** and **S2**, and **SCIN**). These are used in parallel to give the two conditions (**ELHI** and **ELLO**). **ELHI** requires valid
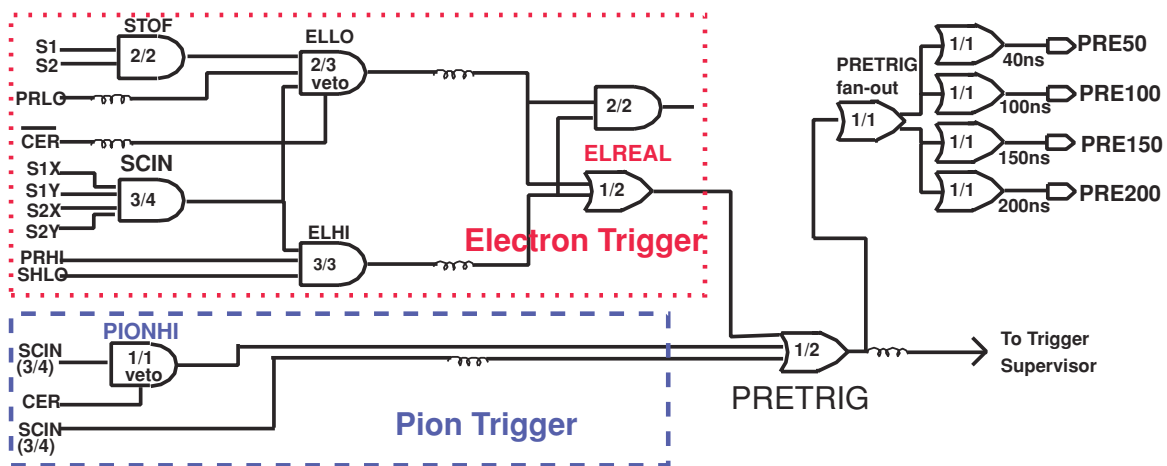

FIG. 5. (Color online) Schematic of the spectrometer pretrigger logic during Fpi-2. The pre-selection of good electron events is accomplished by the upper part of the system, while the lower part is used to select good pion events. The individual triggers from each spectrometer form a pretrigger, which is sent to the trigger supervisor where the signals from the spectrometers are processed and readout of the data is initiated. The split of the **PRETRIG** signal is used to determine the electronic dead time as described in Sec. IV F 3.

scintillator information and sufficiently large signals in the calorimeter (**PRHI** and **SSHLO**), while **ELLO** is satisfied by two of the three signals **STOF**, **PRLO**, and **SCIN**, and the presence of a signal from the gas Cherenkov. In the hadron arm, good pion events were selected by **SCIN** with the additional requirement of no signal above a given threshold in the Cherenkov (**PIONHI**). The threshold for a hit in the Cherenkov was set lower in Fpi-1 than in Fpi-2. Each trigger signal is sent to a TDC and read out by the data acquisition system. This makes it possible to determine the efficiency for a given trigger type. The total trigger efficiency obtained is discussed in Sec. IV F 2.

In the experiment, the number of pretrigger signals formed for each spectrometer and each trigger type are recorded. This makes it possible to calculate the computer dead time for each trigger branch. In addition, the pretrigger signal **PRETRIG** is split into four copies of varying length for determining the electronic dead time (see Sec. IV F 3). In Fpi-1, the signal was split before the **PRETRIG** module into four signals of gate widths 30, 60, 90, and 120 ns; whereas in Fpi-2, it was split afterward into signals of effective gate widths 50, 100, 150, and 200 ns. More detailed information about the trigger setup can be found in Refs. [27,33,34].

The data acquisition software used was CODA (CEBAF on-line data acquisition) version 1.4 [35]. Three types of data were recorded for each run: TDCs and ADCs for the various detectors were recorded event-by-event, scalers for, e.g., the charge were read out every 2 s, and EPICS data from the slow controls were read out at least every 30 s (in some cases, every 2 s). The ADC, TDC, and scaler information is read out over a network through Fastbus and VME crates, each of which had their own readout controller CPU, for each event in the data stream. Both ADCs and TDCs are sparsified. The threshold values of all ADC channels are determined from 1000 artificial events created at the beginning of each run.

IV. DATA ANALYSIS AND CALIBRATIONS

This section describes the determination of the normalized experimental yields, as a function of the relevant kinematic variables, including the necessary calibrations, with special attention to the precision obtained.

A. Beam position and direction

The position and direction of the electron beam incident on the target were carefully monitored during the experiment with the equipment described in Sec. III B.

Deviations in the vertical direction and position of the beam result in offsets of the momentum and out-of-plane angle of the detected particle, while deviations in the horizontal direction of the beam result in an offset in the scattering angle (a deviation in the horizontal position is taken into account by the optical calibration of the spectrometers).

Observed deviations in the vertical position were 0.3 mm, with a stability of better than 0.2 mm, and 0.5 mrad in the directions, with run-to-run variations of less than 0.1 mrad. Corrections for the effect of these deviations were made (see

Sec. IV C). For example, for a 1 mm vertical offset of the beam on the target, the reconstructed momentum and out-of-plane angle in the HMS would shift by 0.08% and 1.1 mrad. The corresponding values for the SOS are 0.04% and 0.4 mrad [34].

B. Target thickness

As mentioned in Sec. III C the nominal target density was 0.0723 ± 0.0005 g/cm^3. The effective target length was calculated as the cryotarget length, measured at room temperature, corrected for thermal contraction (about 0.4% at 20 K) of the aluminum cell walls, the offset of the cryotarget from the nominal position, and for the central position and the rastering of the beam on the target. The latter two corrections were negligible in Fpi-1 thanks to the nearly flat surface of the beer-can type cells used. In Fpi-2, for the largest deviation of the beam from the target center, the correction of the target length was $1.50 \pm 0.05\%$, while the corrections for the rastering of the beam were <0.1%.

The effective target length, not corrected for (run-dependent) beam offsets, corresponding target thickness, and associated uncertainties are listed in Table III. The uncertainty on the nominal target thickness was taken as the quadratic sum of a 0.6% uncertainty on the effective target length and 0.7% on the target density. The variation in target thickness due to the central beam position between high and low ϵ settings was 0.2%.

Although the electron beam was rastered to spread the energy deposited in the target liquid over a larger volume, the target thickness may still be influenced by local target boiling. To measure the effective target thickness, ^{1}H(e, e) elastic scattering data were taken at fixed kinematics for electron beam currents between 10 and 90 μA. A possible target thickness reduction was determined by comparing the dead-time corrected and tracking corrected yields as a function of beam current. To check that rate-dependent effects were properly taken into account, additional data were taken with a solid carbon target during Fpi-2, for which no density reduction effects are expected. The results suggest no current- or rate-dependent effects for carbon at the 10^{-3} level. For the cryogenic hydrogen target, the analysis of Fpi-1 data taken with the horizontal-flow cryotarget and a fast raster amplitude of ±1.2 mm gave a yield reduction of $(6 \pm 1)\%/100$ μA. The Fpi-2 yield reduction for the vertical-flow cryotarget was determined to be $(0.6 \pm 0.1)\%/100$ μA for a raster amplitude of ±2 mm. The improvement in the yield reduction in Fpi-2 compared to Fpi-1 is due to the improved raster design and vertical-flow cryotarget.

TABLE III. Cryotarget lengths and thicknesses, not corrected for beam offsets.

Experiment	Target	L_{target} (cm)	t_{cryogen} (g/cm^2)
Fpi-1	LH$_2$	4.53 ± 0.025	0.328 ± 0.003
Fpi-2	LH$_2$	3.92 ± 0.025	0.283 ± 0.003

C. Optical calibrations

The HMS and SOS were used to determine the momentum vector (magnitude and direction) of the detected particles at the target, as well as to reconstruct the location of the reaction vertex. The reconstruction of the vertex kinematics is achieved by means of a matrix containing the elements of a Taylor expansion of the vertex variables in terms of the focal-plane variables. These variables, which are determined from the drift chamber information, are the positions $x_{\rm fp}$ in the dispersive and $y_{\rm fp}$ in the nondispersive direction, and the directions $x'_{\rm fp}$ and $y'_{\rm fp}$ with respect to the forward z direction, of the particle in the detection (or nominal focal) plane. This plane is about half-way between the two drift chambers (see Sec. III E 1). Both spectrometers feature a point-to-point focus in both the dispersive and nondispersive directions for particles with a central momentum, which is the momentum of a particle that passes through the middle of the entrance quadrupole(s) and the wire chambers (the optical axis) of the spectrometer. The central momentum p_0 is related to the magnetic field of the spectrometer by $p_0 = \Gamma B$. The value of the spectrometer constant Γ is given by the spectrometer design, adjusted on account of calibrations.

The reconstruction is performed with the formula

$$x_{\rm tar}^i = \Sigma_{j,k,l,m}^N M_{jklm}^i (x_{fp})^j (y_{fp})^k (x'_{fp})^l (y'_{fp})^m, \qquad (9)$$

where the M_{jklm}^i denote the elements of the reconstruction matrix. The reconstructed quantities, $x_{\rm tar}^i$ in the target system, are the sideways position $y_{\rm tar}$ in a plane perpendicular to the optical axis at the target, the inclinations $x'_{\rm tar}$ and $y'_{\rm tar}$ with respect to the optical axis, and the momentum p of the particle. The latter is commonly described relative to the central momentum p_0 by using the variable δ:

$$\delta = \frac{(p - p_0)}{p_0}. \qquad (10)$$

The sum over indices is constrained by $0 \leqslant j + k + l + m \leqslant N$, where N is the order of the series expansion. In the reconstruction, it is assumed that $x_{\rm tar} = 0$ and that the vertical spread of the beam at the target can be neglected, which enables one to determine δ (and thus p). Any deviation of $x_{\rm tar}$ from zero, e.g., from rastering the beam, is corrected for using the known optical properties of the spectrometer. The left-right symmetry of the spectrometers restricts the allowed combinations of k and l. For instance, it forces the matrix elements for δ and $x'_{\rm tar}$ to be zero when $k + l$ is odd, while those for $y_{\rm tar}$ and $y'_{\rm tar}$ are zero when $k + l$ is even. If the symmetry is broken, e.g., due to a misalignment of a magnet, the "forbidden" matrix elements may have nonzero values.

The reconstruction matrix elements were fitted by using specially taken calibration data. For determining the $y_{\rm tar}$, $x'_{\rm tar}$, and $y'_{\rm tar}$ matrix elements, data were taken using the quintar and sieve slits (see Secs. III C and III D 1). These slits consist of 3.175 cm thick tungsten plates with holes at regular intervals, providing for discrete values of $x'_{\rm tar}$ and $y'_{\rm tar}$. The quintar gave discrete values of $z_{\rm tar}$, from which the value of $y_{\rm tar}$ can be calculated by using the angle between the target and the spectrometer, and the value of $y'_{\rm tar}$. These data were taken with a continuous particle-momentum spectrum. Discrete momenta
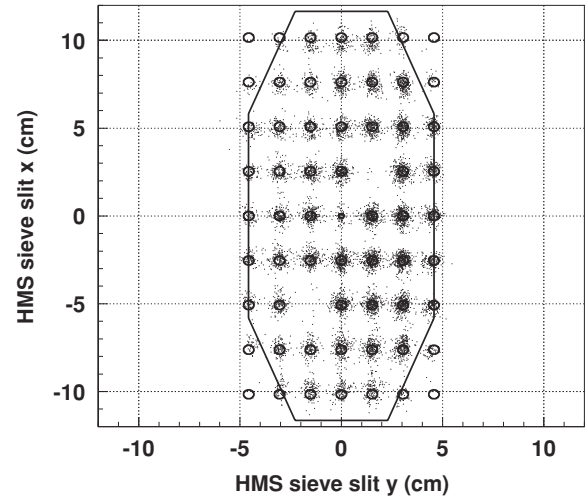

FIG. 6. Reconstruction of the hole pattern of the HMS sieve slit. The central hole is smaller, and some holes are blocked for verifying the orientation. Overlaid is the acceptance as defined by the octagonal collimator. The lack of events in the holes in the corners is caused by limited acceptance. Data from all five quintar positions were added.

for determining the δ matrix elements were obtained by using (in)elastic scattering data on ^{12}C and ^{1}H targets. By changing the central momentum (or the spectrometer angle in the case of the hydrogen target) in discrete steps, the scattered-electron peaks were shifted over the focal plane, thus scanning the entire δ acceptance.

The strengths of the quadrupole fields for a particular field of the dipole magnet (central momentum setting) are selected to obtain point-to-point focusing in both directions for particles traveling along the optical axis ($p = p_0$, $\delta = 0$). In this case, the focus of the beam envelope in the focal plane will be located at $x_{\rm fp} = 0$ and $y_{\rm fp} = 0$. Changes in the magnetic field strength due to saturation effects would manifest in a shift of the focal plane focus. The stability of the focal plane distributions for the HMS was found to be better than ± 0.5 cm for central-momentum settings ranging from 0.8 to 5.0 GeV/c.

The HMS reconstruction matrix was expanded up to fifth order in the fitting. Forbidden matrix elements were included, which improved the reconstruction, especially for $y_{\rm tar}$ and $y'_{\rm tar}$.[1] Figure 6 displays the sieve slit reconstruction of the HMS, overlaid with the nominal hole positions and the area covered by the collimator. The outermost vertical sieve slit holes are at ± 60.5 mrad so that the sieve slit does not entirely cover the acceptance of the octagonal collimator. For particles passing the octagonal collimator beyond this range, the reconstruction relies on the extrapolation of the Taylor series [Eq. (9)] to a region where it has not been fitted, and the resolution worsens considerably. Therefore, only a range of ± 60 mrad in $x'_{\rm tar}$ was used during the analysis of the π^+ data in Fpi-1. To extend

---

[1]It was later found [27] that the breaking of midplane symmetry (which leads to forbidden matrix elements) is most likely caused by a rotation of Q2 by 0.2° around its optical axis. No explicit correction for the effects of this are needed, since the forbidden matrix elements are included in the model of the HMS.
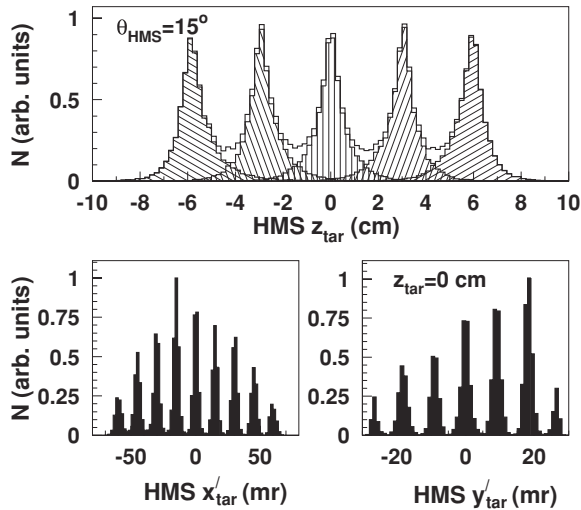
FIG. 7. HMS quintar and sieve-slit reconstruction. Top: reconstruction of the quintar z_{tar} co-ordinate. The distribution shown is the sum of the five individual targets. Bottom: reconstruction of the vertical (left) and horizontal (right) sieve-slit hole patterns (central target foil only).
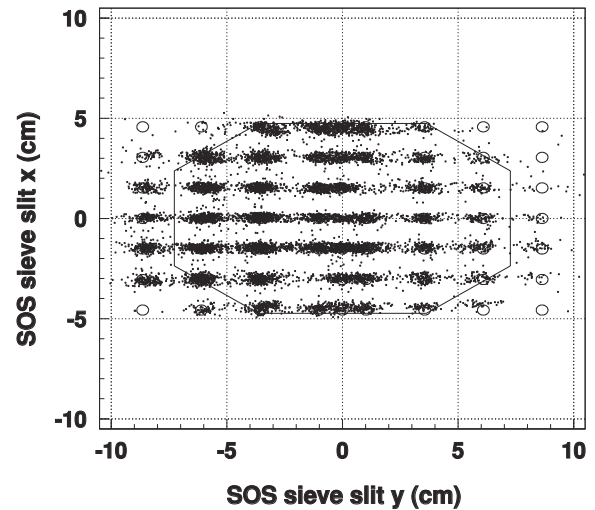

FIG. 8. Reconstruction of the hole pattern of the SOS sieve slit, overlaid with the acceptance as defined by the octagonal collimator. The central hole is smaller, and some holes are blocked for verifying the orientation. The lack of events in the holes in the corners is caused by limited acceptance.

the valid region of the out of plane matrix elements, optics data were taken in 2003 with the sieve slit shifted by one half row, extending the vertical range of the outermost sieve hole columns by ± 1.27 cm. The x'_{tar} matrix elements were then optimized following the procedure outlined in Ref. [34]. In this analysis, the HMS reconstruction matrix was expanded to sixth order.

Figure 7 shows the reconstruction of the z_{tar} position of the five quintar target foils, and the reconstruction of the sieve-slit holes in the vertical (x') and the horizontal (y') directions. The resolutions in x'_{tar} and y'_{tar} were determined by quadratically subtracting the σ of the shape of the holes from the values given above. The resolutions are summarized in Table IV.

The SOS reconstruction matrix was expanded to sixth order. The matrix was first determined in 1997 using optics data taken at $P_{SOS} \approx 1.4$ GeV/c for δ and $P_{SOS} \approx 1.65$ GeV/c for the quintar/sieve-slit data. The reconstruction of the SOS sieve slit is shown in Fig. 8. The top plot in Fig. 9 shows the reconstruction of the positions of the target foils of the quintar target with the SOS positioned at an angle of $20°$ with respect to the beam. The bottom plot shows the sieve-slit pattern for

the central foil of the quintar target. The resolutions are listed in Table IV.

Complications arise due to the resistive nature of the SOS magnets. It was found [27,28] that saturation effects start to play a role for central momentum settings above about 1.0 GeV/c. The effective field length decreases, resulting in a decrease of $p_0/B = \Gamma$. A correction to the central momentum was parametrized based on elastic scattering data from hydrogen, see Fig. 10. The effect can be as large as 1.3% at the maximum central momentum of 1.74 GeV/c.

A second effect of saturation is that it influences the SOS optics. This effect was first observed in Fpi-1 and was
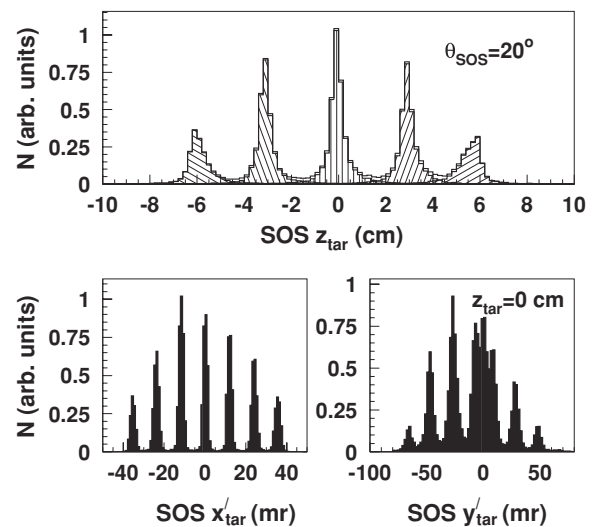
FIG. 9. SOS quintar and sieve-slit reconstruction. Top: reconstruction of the quintar z_{tar} coordinate. The distribution shown is the sum of the five individual targets (hashed). Bottom: reconstruction of the vertical (left) and horizontal (right) sieve-slit hole pattern.

TABLE IV. Resolutions (σ) of HMS at 2.2 and SOS at 1.65 GeV/c. The resolutions x'_{tar} and y'_{tar} are shown for individual holes and for rows and columns of holes to provide information about the size of systematic effects in the sieve-slit reconstruction.

	HMS	SOS
x'_{tar} (indiv. holes)	1.8 mrad	0.3–0.5 mrad
x'_{tar} (columns)	1.8–2.1 mrad	0.3–0.8 mrad
y'_{tar} (indiv. holes)	0.3–0.7 mrad	2.4–2.7 mrad
y'_{tar} (rows)	0.8–1.0 mrad	3.1–3.3 mrad
y_{tar} (mean)	2 mm	0.9–1.1 mm

FIG. 10. Saturation correction for the SOS central momentum. The 2004 data points are from Ref. [37].

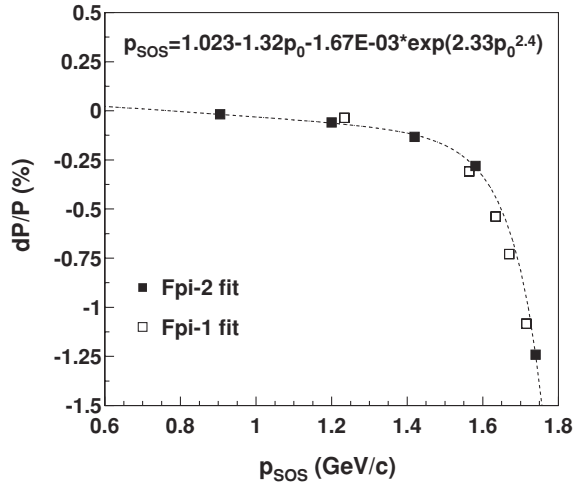addressed with a momentum-dependent correction to δ only, as described in detail in Chap. 4.6 of Ref. [27]. It was addressed in much more detail in Fpi-2 by refitting the optics matrix at different central momenta, thus making the matrix momentum dependent [36]. The main effect was on the determination of δ. The effects on x'_{tar} and y'_{tar} were found to be relatively small, of the order of 1 mrad, as were those on y'_{tar}.

D. Offsets

After the optimization of the matrix elements, as described in Sec. IV C, the spectrometer quantities δ, x'_{tar}, y_{tar}, and y'_{tar} should be reconstructed correctly. However, during the experiment, one should allow for small deviations from the calibration values resulting, e.g., from small variations in the vertical position of the beam and in cycling the spectrometers, and possible saturation effects. Furthermore, small deviations in the electron energy E_e and the central spectrometer angles θ_{HMS} and θ_{SOS} from the nominal values are possible. Most of these experimental offsets can be traced by analyzing single-arm elastic scattering and coincident ${}^1\text{H}(e, e'p)$ data. This reaction is kinematically overdetermined, which allows one to inspect the following quantities:

(i) The invariant mass of the photon-target system W, which should equal the proton mass.
(ii) The missing energy $E_m = E_e - E_{e'} - T_p$, where E_e is the energy of the incoming electron, $E_{e'}$ the energy of the scattered electron, and T_p the kinetic energy of the recoiling proton, which should should be zero.
(iii) The three components p_m^{par}, p_m^{per}, and p_m^{oop} of the missing momentum $\mathbf{p}_m = \mathbf{p}_e - \mathbf{p}_{e'} - \mathbf{p}_p$ (defined as the components parallel to the momentum transfer vector $\mathbf{q} = \mathbf{p}_e - \mathbf{p}_{e'}$, perpendicular to $\mathbf{q}$ in the scattering plane, and out of the scattering plane), which should all be zero.

The seven experimental quantities that are checked are the beam energy E, the momenta of the scattered electron and the recoiling proton $p_{e'}$ and p_p, their angles $\theta_{e'}$ and θ_p,

and their out-of-plane angles $\phi_{e'}$ and ϕ_p. The quantities $\phi_{e'}$ and ϕ_p are related to p_m^{oop}, while the others are related to the four quantities W, E_m, p_m^{par}, and p_m^{per}.

During the experiment, single arm ${}^1\text{H}(e, e')$ and coincidence ${}^1\text{H}(e, e'p)$ runs were taken at each electron energy. These data were analyzed to yield a set of experimental offsets that minimizes the deviations of the values of W, E_m, and $\mathbf{p}_m$ from their theoretical values. In the analysis, the offset in a spectrometer angle was taken to be constant, independent of the spectrometer setting. During Fpi-1, the offset in the beam energy E, with respect to the value determined as described in Section III B, was allowed to be different for each new electron energy. In view of the availability of more precise beam-energy measurements, the beam energy was kept fixed during Fpi-2. Since no saturation effects have been observed in the HMS up to momentum settings of 5 GeV/c, the offset in the HMS spectrometer momentum was taken to be constant for all excitations. For the SOS, the offset was taken to be a function of the central momentum (see Sec. IV C). In fitting the offsets, the effects of radiation and energy loss were taken into account. The effect of the beam not being centered vertically was included as well, because such an offset can mimic a momentum offset.

The experimental offsets found are listed in Table V. The major offsets are those on the spectrometer momenta. With these offsets, the reconstructed values of W, E_m, and $\mathbf{p}_m$ were within 1–2 MeV or MeV/c of their physical values. The intrinsic uncertainties (not including possible correlations between the offsets) in the offsets are $\pm 0.05\%$ for energies and momenta, and ± 0.5 mrad for angles.

The offsets on the electron energies are $<0.15\%$, and the offsets on the in-plane spectrometer angles are <1 mrad. The larger values of the out-of-plane angle offsets have a few origins. First of all, it is known from surveys that the SOS has a 2.6 mrad out-of-plane offset. Furthermore, it was determined afterward that the original calibration data for both the HMS and SOS had been taken with a vertical offset of the beam. This influences especially the ϕ offset of HMS. During Fpi-1, no corrections were made for a vertical offset of the beam during the data taking, but the effect was accounted for in the ϕ offsets of both the HMS and SOS. During Fpi-2, such corrections were included. The remaining ϕ offsets of 1.1 and 0.6 mrad mainly result from the mentioned offset during the original calibrations.

The Fpi-2 offsets include no offset in the HMS central angle (compared to the previously used angle offset of 1 mrad). The Fpi-2 HMS kinematic offsets are in relatively good agreement with elastic electron singles data from 1999 [38] and with data taken in 2004 [37]. The difference in the values found

TABLE V. Kinematic offsets.

Quantity	HMS Fpi-1 (Fpi-2)	SOS Fpi-1 (Fpi-2)
θ	+1.0 (0.0) mrad	−0.4 (0.0) mrad
ϕ	+2.4 (+1.1) mrad	+2.6 (+3.2) mrad
p_0	−0.33 (−0.13) %	0.0 to −1.1 (0.0 to −1.4)%
E_e	−0.15 to +0.14% (0.0)	

for Fpi-1 and Fpi-2 may partly be due to a small difference in the direction of the incoming beam. Also for the HMS, which was used to detect the scattered electron, there is a strong correlation between the offsets found for θ and for p_0. When using the Fpi-2 offsets for the data taken during Fpi-1, an only slightly worse description is found.[2] As described in Sec. IV C, the large momentum-offset values for SOS result from saturation effects.

E. Particle identification and event selection

Electrons were identified in the SOS using the gas Cherenkov and calorimeter. Electron events were selected with a Cherenkov cut of $N_{\text{photoelectrons}} > 0.5$ and a calorimeter cut $E/p > 0.6$ (Fpi-1) or 0.7 (Fpi-2). The relatively low photoelectron cut used resulted in several π^- passing particle identification. However, when combining these with a π^+ in the HMS, almost all of them were random coincidences and removed by the random subtraction. The loss of electrons due to these cuts was <0.1%, whereas the online suppression of pions was better than 99%. After offline analysis, the pion contamination was <0.03% in all cases.

In the HMS, where π^+ were detected, the contaminating particles were protons and positrons. During Fpi-1, an upper limit of 0.2 photoelectrons in the Cherenkov detector provided a positron rejection of >99.4%, resulting in a final positron contamination of <0.02%. The loss of pions at this limit was 3.1%. Proton rejection was accomplished via the particle speed, $\beta = v/c$, calculated from the time-of-flight difference between the two hodoscopes in the HMS detector stack. With the chosen cut of $\beta > 0.925$, the loss of pions is negligible.

During Fpi-2, no offline Cherenkov detector cuts were applied to eliminate positrons, as those that passed particle identification cuts were removed by the subtraction of random coincidences in the analysis (see Sec. IV G). During Fpi-2, the pion and proton momenta were high, resulting in β distributions for pions and protons which were not completely separated, and the HMS aerogel Cherenkov was used to provide additional discrimination. The aerogel Cherenkov efficiency was determined from π^- production data with tight cuts on the missing mass and the calorimeter to eliminate electrons, and was found to be 99.5±0.02% for a threshold cut of $N_{\text{photoelectrons}} > 3$ (the mean number of photoelectrons being 12).

Protons passing the particle identification cuts were effectively removed by the subtraction of random coincidences. Real proton coincidences were avoided via coincidence time cuts (Sec. IV G).

F. Efficiencies

In calculating the normalized yield, one must apply corrections for inefficiencies resulting, e.g., from track reconstruction

and data acquisition dead time. Various efficiencies are discussed in detail in the sections below.

1. Tracking efficiency

As described in Sec. IV C, the basis of kinematic reconstruction is to find a valid track in the pair of drift chambers in each spectrometer. Each chamber has six planes of wires, and a signal in at least five planes is required by the tracking algorithm to start constructing a track for a given event. The tracking algorithm performs a χ^2 minimization by fitting a straight line through both chambers. In case the fit results in more than one possible track, the track that comes closest to the scintillator paddle in the second hodoscope that fired is selected (this feature was not yet implemented during Fpi-1). The complete hierarchy of selection criteria is described in detail in Ref. [39]. Projecting the fitted track to the nominal focal plane yields the position $(x_{\text{fp}}, y_{\text{fp}})$ and direction $(x'_{\text{fp}}, y'_{\text{fp}})$ of the particle.

The tracking efficiency is defined as the probability that the tracking algorithm found a valid track for a particle identified as an electron (or pion). It depends both on the efficiency of the wire chambers and on the tracking algorithm. The particle identification requirements eliminate the bias introduced by the presence of other particle types in the acceptance with possible intrinsic lower efficiency. The HMS tracking efficiency was generally above 98% (Fpi-1) or 97% (Fpi-2) and was only weakly dependent on the event rate. During Fpi-1, the SOS tracking efficiency was slightly worse but still generally above 96%, while during Fpi-2 it was about 99%. This improvement is largely due to the improved tracking algorithm used. The difference between HMS and SOS mainly reflects the difference in incident count rates.

At high rates, there is a nonzero probability for more than one particle to pass through the drift chambers within the approximately 200 ns TDC window used in the analysis. The tracking algorithm determines only one "best" track for each event. Any additional tracks are accounted for by either the electronic or computer dead-time corrections. However, it has been observed that the efficiency for finding a single track is actually significantly lower in the presence of multiple real tracks (this is due to software limitations when dealing with many hits). The rate dependence of the tracking efficiency then mostly comes about from the increased probability of having multiple tracks at high rates. To resolve this issue, a tracking efficiency calculation, including multiple track events, was developed (see Ref. [40] for details).

2. Trigger efficiency

The trigger (see Sec. III F) used for pions in the HMS is largely determined by the scintillators (plus absence of the Cherenkov signal), so the trigger efficiency can be expressed directly in terms of the efficiency of the separate scintillator signals. For SOS, the total trigger efficiency is given by the product of scintillator, calorimeter, and gas Cherenkov efficiencies.

---

[2]Checks have shown that because of the correlation in these offsets, the uncertainty in them has an almost negligible influence on the final ^{1}H($e, e'\pi^+$)n results, see Sec. V C.

The needed three out of four scintillator efficiency for either spectrometer can be written as

$$P_{\frac{3}{4}} = P_1 P_2 P_3 P_4 + P_1 P_2 P_3 (1 - P_4) + P_1 P_2 (1 - P_3) P_4$$
$$+ P_1 (1 - P_2) P_3 P_4 + (1 - P_1) P_2 P_3 P_4, \quad (11)$$

where P_i denotes the single-plane efficiency for each scintillator plane. The individual plane efficiencies can be calculated from the number of times a valid track that gives a valid hit in three planes produces a signal in the paddle of the fourth plane it intersects. To minimize the track dependence of the efficiency, adjacent paddles to the one that should have fired are included in the calculation.

The variation of the 3/4 efficiency across the spectrometer acceptance is also of great importance, since different parts of the acceptance feed different parts of the phase space. This was investigated for HMS during Fpi-2. The 3/4 efficiency was determined for both HMS e-p elastic and pion electroproduction data. In both cases, an inefficiency of 1.5% was found at negative fractional momentum, $\delta < -5.0\% (-8.0\%)$, outside the region used in the analysis of the Fpi data. Within that region, the efficiency was $99.85 \pm 0.05\%$.

3. Computer and electronics dead times

The computer dead time can be directly calculated from the number of (generated) pretriggers and (accepted) triggers. The computer dead time was relatively large during Fpi-1 because the data acquisition system was used in an unbuffered mode to avoid potentially serious synchronization problems. The event rate was commonly chosen such that computer dead time was below 40%. The computer dead time during Fpi-2 was about 10%.

The computer dead time at high rates was tested using data taken at fixed current and varying computer dead times. The resulting normalized and corrected yields at different live times agreed within 0.2%, which number was taken as the uncertainty in the computer live time.

While the computer dead time can be directly measured, the electronics dead time was estimated from copies of the original pretrigger signal at varying limiting gate widths. This was done using four scalers with different gate widths (30, 60, 90, and 120 ns in Fpi-1, and 40, 100, 150, and 200 ns in Fpi-2). The true limiting gate width in the trigger logic corresponds to the width of the pretrigger output and was effectively about 50 ns for Fpi-1 and 60 ns for Fpi-2. Knowing the rates and the lengths of the gates of the four scalers, the effective limiting gate width τ can be determined, and hence the correction can be calculated for electronics dead time, using the formula $\epsilon_{el.d.t.} = 1 - R\tau$, where R is the actual event rate. The corrections were at most 3% (for high rates in the HMS during Fpi-2), with an overall uncertainty of 0.1%, calculated from an estimated uncertainty of the gate widths of HMS and SOS.

4. Coincidence blocking

The coincidence time between the spectrometers is used in the analysis to define good coincidence events. Such a coincidence event will normally be started at the TDC with a delayed HMS trigger and stopped by the SOS. However, because of interference between noncoincident and coincident events, a fraction of events are recorded with a value of coincidence time outside the main timing window as defined by the pretrigger signal widths. These "coincidence blocking" events will be lost from the data because of the coincidence time cuts used in the analysis. The coincidence blocking correction was estimated from the rate dependence of the number of blocked events. The values range from 99.5% to 99.9% with an uncertainty of about 0.1%.

5. Pion absorption and β efficiency

A fraction of the produced pions are lost as a result of nuclear interactions in the materials that they traverse before reaching the detectors in the HMS detector hut. The loss is mainly due to absorption and large-angle scattering.

Since the absorption cross sections for protons and pions are rather similar for momenta around 2 GeV/c, in Fpi-1, the absorption was estimated based on the difference in yield for simultaneously measured ^{1}H(e, e') and ^{1}H$(e, e'p)$ reactions, yielding a value of $(4.0 \pm 1.5\%)$. In Fpi-2, the transmission of pions through the spectrometer was calculated using the list of traversed material and the pion-nucleon reaction cross section, which includes absorption and inelastic reactions. The calculated transmission for pions with momenta of 2.93 and 3.34 GeV/c was 95%, with an estimated uncertainty of 2%. The reduced pion transmission compared to Fpi-1 is mainly due to the thicker (titanium) spectrometer exit window and the addition of the aerogel Cherenkov in the detector stack.

The situation is complicated by the following. In the analysis, a cut is used on β-β_p, where β is the particle velocity determined from the time of flight between the two scintillator hodoscopes, and β_p is the velocity calculated from the particle momentum. As can be seen in Fig. 11, there is a "tail" in the coincidence time spectrum at low β-β_p, which results mainly
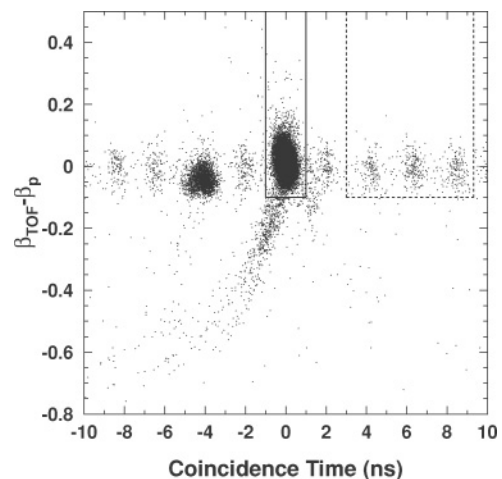

FIG. 11. Coincidence time spectrum taken during Fpi-2, with the used real (solid) and random (dashed) coincidence time cuts. Real proton coincidences are clearly visible but are rejected by the coincidence time cut. The tail is due to π^+ interactions in the detector elements, as explained further in the text.

from pions undergoing nuclear interactions in the scintillators, aerogel, or Cherenkov detector material. The produced slower hadrons are identified as pions, but generally have a larger time of flight. Furthermore, there are pion events with $\beta = 0$, meaning that no hits in the relevant scintillators were found when projecting the reconstructed track to the hodoscopes, which may also result from scattering of the pion.

The corrections for $\beta = 0$ and the tail events were slightly different in Fpi-1 and Fpi-2. While the tail was neglected in Fpi-1, it was corrected for in Fpi-2. The latter approach includes the possibility of double-counting, when the tail particle was due to a pion that reacted in the material, which was explicitly corrected for in the absorption calculation. Therefore, the absorption of pions and the various contributions in the β-β_p spectrum were studied in more detail by calculating the number of pions reacting in various parts of the traversed material (also including elastic scattering), and estimating which fractions of these end up in the β-β_p vs coincidence-time spectrum and where in that spectrum. These studies were also performed for protons, where the absorption could be determined experimentally by comparing single (e, e) and coincident $(e, e' p)$ events in the elastic peak in the measurements on the ^{1}H$(e, e' p)$ reaction. The results indicated that the total transmission plus detection efficiencies for the used cuts differed by $+1.8\%$ for Fpi-1 and -0.7% for Fpi-2 from what had been used in the analysis. Since this is within the assumed uncertainty of the efficiency correction and well within the overall uncertainty of the final separated cross sections, no additional correction was applied.

G. Backgrounds

The coincidence timing structure between unrelated electrons and protons or pions from any two beam bursts is peaked every 2 ns because of the accelerator timing structure. Real and random e-π coincidences were selected with cuts placed as shown in Fig. 11. The random coincidence background during Fpi-1 was 2–5%, depending on the kinematic setting, while it was always <1% during Fpi-2.

The contribution of background events from the aluminum cell walls was estimated using dedicated runs with two "dummy" aluminum targets placed at the appropriate z positions (see Sec. III C). These data were analyzed in the same way as the cryotarget data, and the yields were subtracted from the cryotarget yields, taking into account the different thicknesses (about a factor of 7) of the target-cell walls and dummy target. The correction was small (2–4.5%), and thanks to the high statistical accuracy of the dummy-target data, the contribution of the subtraction to the total uncertainty was negligible.

H. Missing mass

The reconstructed missing mass M_m, see Fig. 14, provides an additional check on all momentum and angle calibrations. With the calibrations and offsets discussed in Secs. IV C and IV D, the values of the missing mass for the various kinematic cases were within 2 MeV of the neutron mass (with correction

for radiative effects, see Sec. V B). In the analysis, a cut on the missing mass of $0.92 < M_m < 0.98$ GeV was used to ensure that no additional pions were produced. The missing mass range was chosen in a region where the distribution is nearly flat (20 MeV above the missing mass peak), and resolution has a minimal effect on the yield, and errors from insufficient simulation of radiative processes at higher missing mass have not yet set in. Therefore, the result does not depend on the cut on the missing mass.

V. DETERMINATION OF THE CROSS SECTION

A. Method

As described in Sec. II B, the (reduced) cross section can be written as a sum of four separate cross sections or structure functions, which depend on W, Q^2, and t,

$$2\pi \frac{d^2\sigma}{dt\,d\phi} = \frac{d\sigma_{\mathrm{T}}}{dt} + \epsilon \frac{d\sigma_{\mathrm{L}}}{dt} + \sqrt{2\epsilon(1+\epsilon)}\frac{d\sigma_{\mathrm{LT}}}{dt}\cos\phi$$
$$+ \epsilon \frac{d\sigma_{\mathrm{TT}}}{dt}\cos 2\phi. \qquad (12)$$

To be able to separate the different structure functions, one has to determine the cross section at both high and low ϵ as a function of the angle ϕ for fixed values of W, Q^2, and t. Since the t dependence is important, this should be done for various values of t at every central Q^2 setting. Therefore, the data are binned in t and ϕ, thus integrating, within the experimental acceptance, over W and Q^2, and also over θ_π (the latter is of relevance, since the interference structure functions include a dependence on $\sin\theta_\pi$). However, the average values of W, Q^2, and θ_π generally are not the same for different ϕ and for low and high ϵ. Moreover, the average values of W, Q^2, t, and θ_π, only three of which are independent, may be inconsistent.

Both problems can be avoided by comparing the measured yields to the results of a Monte Carlo simulation for the actual experimental setup (see the next section), in which a realistic model of the cross section is implemented. At the same time, effects of finite experimental resolution, pion decay, radiative effects, etc., can be taken into account. When the model describes the dependence of the four structure functions on W, Q^2, t, θ_π sufficiently well, i.e., when the ratio of experimental to simulated yields is close to unity within the statistical uncertainty and does not depend on these variables anymore (except for a small linear dependence), the cross section for any value of $\overline{W}$, $\overline{Q^2}$ within the acceptance can be determined as

$$\left(\frac{d^2\sigma}{dt\,d\phi}(t,\phi)\right)_{\overline{W},\overline{Q^2}}^{\mathrm{exp}} = \frac{Y_{\mathrm{exp}}}{Y_{\mathrm{sim}}}\left(\frac{d^2\sigma}{dt\,d\phi}(t,\phi)\right)_{\overline{W},\overline{Q^2}}^{\mathrm{model}}, \quad (13)$$

where Y is the yield over W and Q^2, but common values of $\overline{W}$, $\overline{Q^2}$ (if needed to be different for different values of t) can be chosen for all values of ϕ and for the high and low ϵ data, so as to enable a separation of the structure functions. In practice, the data at both high and low ϵ were binned in $5t$ bins and 16ϕ bins, and the cross section was evaluated at the center of each bin. The overlined values in the expression above were taken as the acceptance weighted average values for all ϕ bins

(at both high and low ϵ) together, which results in their being slightly different for the five t bins.

B. SIMC

The Hall C Monte Carlo package SIMC has been used in the analysis of several previous experiments and is described in detail elsewhere (see, e.g., Refs. [27,28]). Only the key components (radiation, hadron decay, spectrometer optics, and multiple scattering) are presented here.

For each event, the program generates the coordinates of the interaction vertex (x, y, z) and kinematic properties such as direction and momentum of the particles of interest. All angles are generated in the spectrometer coordinate system, where z points in the direction of the beam, x is vertical with $x > 0$ pointing downward, and y completes the right-handed coordinate system. The starting values for the generation are limited to a certain range, given as input. When an event is kinematically allowed, the event is radiated and the outgoing particles are followed on their way through the target, taking into account energy loss and multiple scattering.

After the event generation is complete, the events are sent to the single arm spectrometer modules, which simulate the magnetic optics inside the Hall C spectrometers using COSY [41] generated matrix elements,[3] trace the particles through the magnetic fields, and reject events that fall outside of several apertures along the spectrometer. Simulated events that clear all apertures and cross the minimum number of detectors in the detector huts are considered to produce a valid trigger and are reconstructed. The target quantities are reconstructed as described in Sec. IV C, with realistic wire chamber resolutions and reconstruction matrix elements that are consistent with those used to trace the particles through the spectrometers. Generally, the Monte Carlo simulation describes the data quite well (see Fig. 12), except for small regions at the edges of the y'_{tar} acceptance. A similar effect was observed in elastic scattering data. The y_{tar} acceptance is not as well described. This quantity does not, however, contribute to the calculation of any physics quantities and was thus not further optimized. Since only apertures are simulated, no inefficiencies are assigned in the event simulation. Finally, each event is weighted by the relevant model cross section (see Sec. V B 3) corrected for radiative processes, the overall luminosity, and a Jacobian taking into account the transformation between spectrometer and physics coordinates.

The reconstructed quantities are used in the comparison of the simulated and experimental distributions of various variables, an example of which is shown in Fig. 13. If the detector setup is realistically simulated, the boundaries of measured and simulated distributions should match. Differences in magnitude can be attributed to differences between the actual cross section and the one used in the model.

Radiative effects describing the emission of real or virtual photons are an important part in the analysis of electron
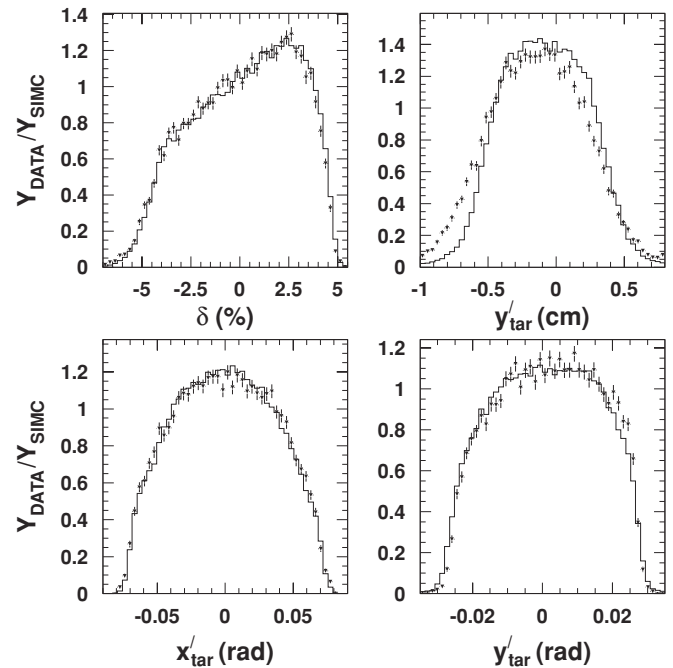

FIG. 12. Comparison of data (triangles) and SIMC (histogram) for HMS reconstructed quantities. The distributions were normalized to each other by one global scale factor.

scattering data. The radiative corrections used in this analysis are based on the formalism of Ref. [42] and include both external and internal radiation. The original formalism, derived for inclusive electron scattering, was extended for $(e, e'p)$ coincidence reactions in Ref. [43].
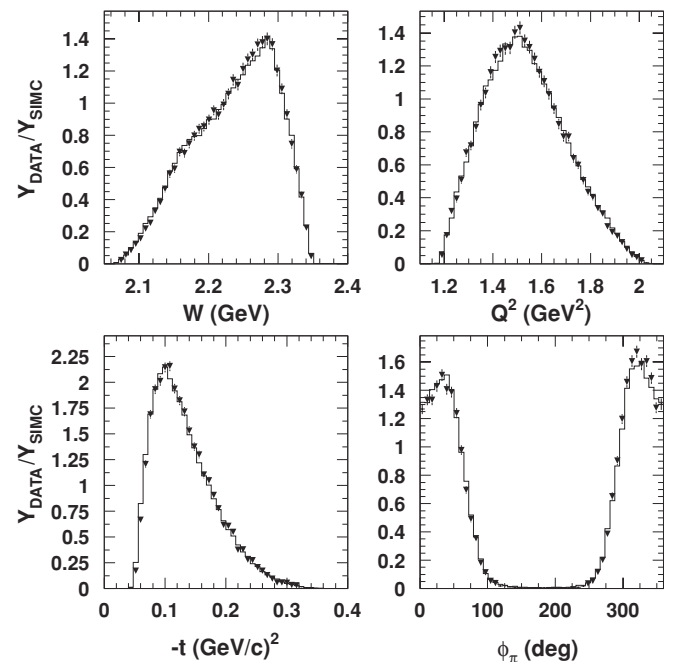

FIG. 13. Comparison of data (triangles) and SIMC (histogram) for the quantities W, Q^2, $-t$, and ϕ_π. The distributions were normalized to each other by one global scale factor.

---

[3]The COSY model consists of sets of "forward matrix elements," which model the magnetic field in steps from one aperture to the next.
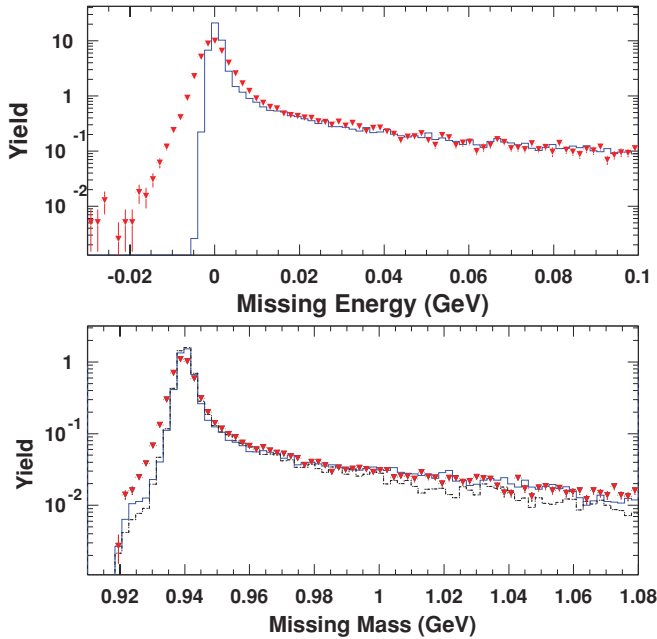
FIG. 14. (Color online) Comparison between data (triangles) and SIMC (histogram) for the missing-energy distribution for one of the ^{1}H$(e, e'p)$ kinematics (top) and for the missing-mass distribution for a representative ^{1}H$(e, e'\pi^+)n$ case (bottom). The solid histogram includes radiative effects and pions that pass through the HMS collimator. The latter events produce an additional contribution in the region $M_m = 1.025–1.07$ GeV. The dashed histogram represents simulated events without the effect of collimator punch-through.

In calculating radiative processes for pion electroproduction, the target particle is a stationary proton, and the final pion is taken to be an off-shell proton. The contribution from two-photon exchange diagrams is not included but is expected to be very small [44]. The energy of the radiated photon is restricted to be much smaller than the energies of the initial and final state particles (soft photon approximation), and the radiation is taken to be in three discrete directions: along the direction of the incoming electron, of the scattered electron, and of the pion (extended peaking approximation).

The method described above has been tested with ^{1}H$(e, e'p)$ data [43,45]. An example for both ^{1}H$(e, e'p)$ and ^{1}H$(e, e'\pi^+)n$ from the present experiment is shown in Fig. 14. The discrepancy at low missing energy for the ^{1}H$(e, e'p)$ case is due to an imperfect simulation of the resolution and peak shape in the tail. However, this does not influence the tail region. The simulated radiative tail gives a good description of the measured one. The global uncertainty is taken to be 2%; in the case of pion production, an additional uncertainty of 1% takes into account the uncertainty associated with the extension of the formalism to pion electroproduction. The differential uncertainty in the L/T separation due to the radiative corrections was estimated by studying the integrated data/SIMC ratio as a function of the missing mass cut for different values of ϵ. Although this ratio was found to vary up to 1.6% when the cuts were applied, the dependence of the ratio on ϵ was relatively small. Based on these studies, a random uncertainty of 0.5% between ϵ settings was assigned.

Charged pions decay into muons and (anti)neutrinos with a branching fraction of 99.99%. The fraction of pions decaying on their way from the target to the detection system depends on their momentum and the path length and was calculated to be up to 20% for the lowest pion momenta. The possibility of pion decay in flight is included in SIMC, which accounts for events lost and for produced muons that still generate a valid trigger. A large fraction of the detected muons come from pion decay close to the target or pion decay in the field free region after the HMS magnetic elements and inside the spectrometer hut. About 4% of the events detected in the spectrometer result from pions that have decayed in flight. The overall uncertainty due to the simulation of pion decay was taken to be 1%. Since the pion momentum distributions are very similar between high and low ϵ settings, the random uncertainty between ϵ settings is very small (about 0.03%), mainly accounting for muons coming from pions normally outside the acceptance.

1. Checks with ^{1}H$(e, e'p)$

In addition to providing information on experimental offsets (see Sec. IV D), the elastic ^{1}H$(e, e'p)$ reaction also serves to check the accuracy of the phase-space model in SIMC; and since the elastic cross section is well known, it can be used to study the accuracy of the calculated yields.

In Fpi-1 (Fpi-2), data for the elastic ^{1}H$(e, e'p)$ reaction were taken in five (four) different kinematic settings, all of which were modeled in SIMC. The experimental and simulated missing energy distributions for one of the settings were already shown in Fig. 14. Other simulated distributions were also in good agreement with the experimental data in all cases except for the kinematic setting in which the SOS is at an angle of 56°. It was found that the model for the SOS in SIMC does not describe correctly the acceptance for part of the events when $|y_{\text{tar}}|$ becomes large (see Sec. V B 2). When that particular region of the phase space was removed from the analysis, the agreement was similar to that for the other kinematics.

The total measured and simulated yields are compared in Fig. 15. The elastic cross sections used in the simulation were taken from the fit to the world data of Ref. [46] for Fpi-1. For Fpi-2, the improved fit from Ref. [47] was also considered. In the region of interest, differences between the two are less than 2.0%. Over the whole Q^2 range between 1.5 and 5.4 GeV^2, the ratio scatters around unity with $\sigma = 2.0\%$, consistent with the uncertainty of the individual points. In addition, one should take into account the uncertainty of the world's data, which is of comparable magnitude.

These results demonstrate that the efficiencies and dead times used to calculate the experimental yields are well understood, and that the Monte Carlo program simulates the experimental conditions and acceptances very well.

2. Detector acceptances in SIMC

In the ^{1}H$(e, e'p)$ reaction, the outgoing electron and proton are strongly correlated, so that only a subset of the phase space is populated. The full SOS acceptance was studied by measuring deep-inelastic electron scattering from deuterium.
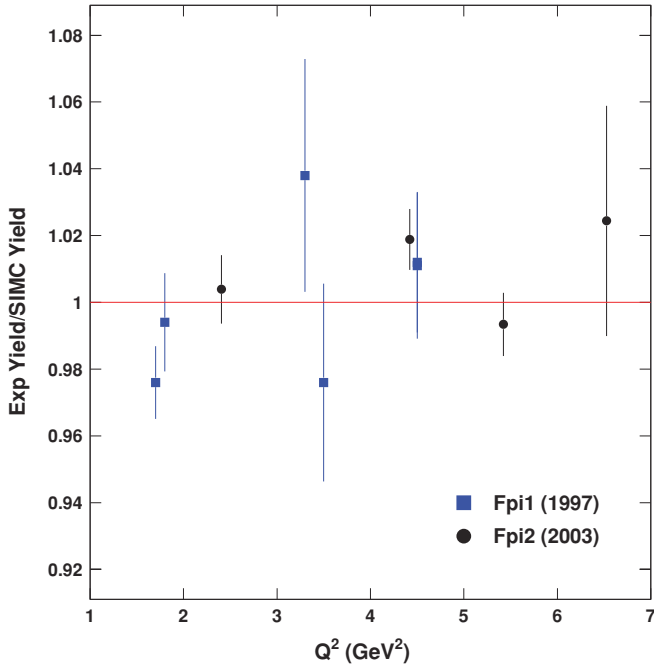
FIG. 15. (Color online) Yield ratios from elastic data and SIMC for Fpi-1 and Fpi-2. The error bars include statistical uncertainties only. The systematic uncertainty is about 2%.

A detailed comparison of the boundaries of the acceptance of the experimental and the simulated data in the four target variables δ, $y_{\rm tar}$, $x'_{\rm tar}$, and $y'_{\rm tar}$ (see Sec. IV C) revealed that in the region

$$y'_{\rm tar} > (-125.0 + 4.25\delta + 64.0 y_{\rm tar} - 1.7\delta y_{\rm tar})$$

and

$$y'_{\rm tar} < (125.0 - 4.25\delta + 64.0 y_{\rm tar} - 1.7\delta y_{\rm tar}),$$

with $y'_{\rm tar}$ in mrad, $y_{\rm tar}$ in cm, and δ in %, the boundaries did not match, with SIMC losing events that were present in the data. Therefore, these parts of the acceptance were excluded from the analysis.

The model for the HMS acceptance does not present a comparable challenge. As the HMS is placed at very forward angles in all kinematics, the $y_{\rm tar}$ acceptance is flat in the (limited) region of interest. The acceptances in $y'_{\rm tar}$ and δ used in the analysis are within the previously determined safe boundaries. The phase space (boundaries) for coincident HMS and SOS events was checked with data from the pion electroproduction reaction by comparing distributions for quantities such as HMS and SOS reconstructed target variables, W, Q^2, t, and missing energy and momenta, see Figs. 12, 13, and 15.

The uncertainties due to spectrometer acceptance were tested by varying the cuts on the quantities (δ, $x'_{\rm tar}$, $y'_{\rm tar}$) in each spectrometer. The experimental cross section was then extracted for spectrometer cut variations of $\pm 10\%$ and compared with the one with nominal cuts. In general, the variation of the cross section is small (<0.5%).
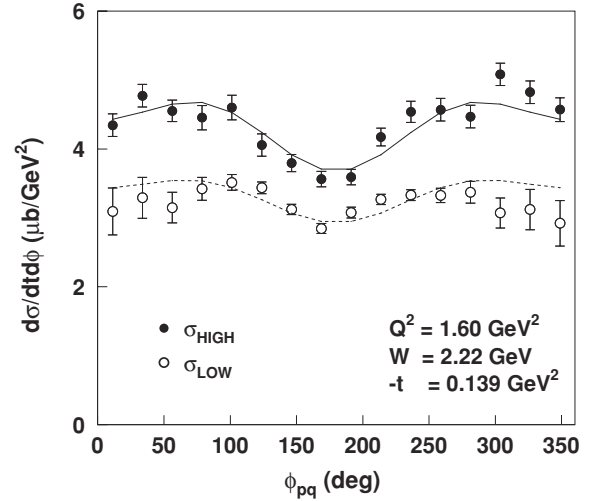

FIG. 16. Representative plot of the experimental cross sections, $\frac{d^2\sigma}{dt\,d\phi}$ as a function of the azimuthal angle ϕ_π at $Q^2 = 1.60$ (GeV^2) for high and low ϵ. The curves represent the fit of the measured values of the cross section to Eq. (12).

3. The model cross section

The model cross section and the final separated structure functions were determined in the same (iterative) procedure. The model cross section was taken as the product of a global function describing the W dependence times (a sum of) Q^2- and t-dependent functions for the different structure functions. For the LT and TT parts, their leading-order dependence on $\sin(\theta^*)$ was taken into account [14]. The W dependence was taken as $(W^2 - M_p^2)^{-2}$, based on analyses of experimental data from Refs. [5,7]. For the parts depending on Q^2 and t, phenomenological forms were used, and the parameters were fitted. For all five t bins at every (central) Q^2 setting, ϕ-dependent cross sections were determined at both high and low ϵ for chosen values of $\overline{W}$, $\overline{Q}^2$ (and corresponding values of θ_π and ϵ) according to

$$\sigma_{\rm exp}(\overline{W}, \overline{Q}^2, t, \phi; \overline{\theta}, \overline{\epsilon}) = \frac{\langle Y_{\rm exp}\rangle}{\langle Y_{\rm sim}\rangle} \sigma_{\rm MC}(\overline{W}, \overline{Q}^2, t, \phi; \overline{\theta}, \overline{\epsilon}). \quad (14)$$

The fitting procedure was iterated until $\sigma_{\rm exp}$ changed by less than a prescribed amount (typically 1%). A representative example of the experimental cross section and the fit as a function of ϕ_π is shown in Fig. 16. The cosine structure from the interference terms is clearly visible.

This procedure was carried out independently for Fpi-1 and Fpi-2 in order to have optimal descriptions in the two different kinematic ranges covered.[4] The final cross section parametrization for Fpi-1 (the cross sections have units of μb/GeV^2, and the units of Q^2, t, and m_π^2 are GeV^2) is

$$\frac{d\sigma_L}{dt} = 36.51 e^{(26.10 - 7.75Q^2)(t+0.02)},$$

$$\frac{d\sigma_T}{dt} = \frac{0.74}{Q^2} + \frac{1.25}{Q^4} + 0.57 \frac{|t|}{(|t| + m_\pi^2)^2},$$

---

[4]These parametrizations are for a nominal value of $W = 1.95$ GeV.

$$\frac{d\sigma_{\mathrm{LT}}}{dt} = \left(\exp\left[4.69 + \frac{24.55}{\sqrt{Q^2}}t\right] + 1.47 - \frac{7.89}{Q^4}\right)\sin\theta^*,$$

$$\frac{d\sigma_{\mathrm{TT}}}{dt} = \left(\frac{3.44}{Q^2} - \frac{7.57}{Q^4}\right)\frac{|t|}{\left(|t| + m_\pi^2\right)^2}\sin^2\theta^*. \qquad (15)$$

This parametrization is valid in the Q^2 range between 0.4 and 1.8 GeV^2.

The Fpi-2 parametrization, valid between $Q^2 = 1.4$ and 2.7 GeV^2, is

$$\frac{d\sigma_{\mathrm{L}}}{dt} = \frac{350Q^2}{(1 + 1.77Q^2 + 0.05Q^4)^2}e^{(16-7.5\ln Q^2)t},$$

$$\frac{d\sigma_{\mathrm{T}}}{dt} = \frac{4.5}{Q^2} + \frac{2.0}{Q^4},$$

$$\frac{d\sigma_{\mathrm{LT}}}{dt} = \left(\exp\left[0.79 + \frac{3.4}{\sqrt{Q^2}}t\right] + 1.1 - \frac{3.6}{Q^4}\right)\sin\theta^*, \qquad (16)$$

$$\frac{d\sigma_{\mathrm{TT}}}{dt} = -\frac{5.0}{Q^4}\frac{|t|}{\left(|t| + m_\pi^2\right)^2}\sin^2\theta^*.$$

Since the extracted separated cross sections depend in principle on the cross section model, there is a "model" systematic uncertainty. This uncertainty was studied by extracting σ_{L} and σ_{T} with different cross section models. Since the longitudinal and transverse cross sections in the model reproduce the experimental values to within 10%, these two terms were independently increased and decreased by 10% in the model. With these changes, the extracted σ_{L} and σ_{T} varied by less than 0.5%. For evaluating the model uncertainty due to the interference terms σ_{LT} and σ_{TT}, these terms were independently increased or decreased by their respective uncertainties, obtained when fitting the four structure functions, and L/T separations were done with the modified models. The contribution to the uncertainty of σ_{L} and σ_{T} of these two terms is between 1% and 8% and depends strongly on t. The latter value (at the largest values of $-t$) is comparable to the contribution of uncorrelated uncertainties to σ_{L} and σ_{T}.

C. Estimate of uncertainties

The statistical uncertainties in the unseparated cross sections are determined by the uncertainties in $Y_{\exp}$ and Y_{sim} in Eq. (13). The statistical uncertainty in $R = Y_{\exp}/Y_{\mathrm{sim}}$ is dominated by the uncertainty in the number of measured real events, and it ranges from 1% to 3%, depending on the values of Q^2 and t.

The systematic uncertainties can be subdivided into correlated and uncorrelated contributions. The correlated uncertainties, i.e., those that are the same for both ϵ points, such as target thickness corrections, are attributed directly to the separated cross sections. Uncorrelated uncertainties are attributed to the unseparated cross sections, with the result that in the separation of σ_{L} and σ_{T} they are inflated, just as the statistical uncertainties, by the factor $1/\Delta\epsilon$ (for σ_L), which is about 3. The ϵ-uncorrelated uncertainties can be subdivided

TABLE VI. Summary of systematic uncertainties for Fpi-2. Where two values are given, they are for the two Q^2 points. When a range is given, it corresponds to the range in t values. The last column gives the sections where the various items are discussed. For Fpi-1, only the total uncertainties are listed, because the individual contributions are similar to those for Fpi-2.

Correction	Uncorr. (pt-to-pt) (%)	ϵ uncorr. t corr. (%)	Corr. (scale) (%)	Sec.
Acceptance	1.0 (0.6)	0.6	1.0	V B2
Model dep.	0.2	1.1–1.3	0.5	V B3
$d\theta_e$	0.1	0.7–1.1		IV D
dE_{beam}	0.1	0.2–0.3		IV D
dP_e	0.1	0.1–0.3		IV D
$d\theta_\pi$	0.1	0.2–0.3		IV D
Radiative corr		0.4	2.0	V B
Pion absorption		0.1	2.0	IV F5
Pion decay	0.03		1.0	V B
HMS tracking		0.4	1.0	IV F5
SOS tracking		0.1	0.5	1V F1
Charge		0.3	0.4	III B
Target thickness		0.2	0.9	IV B
CPU dead time		0.2		IV F3
HMS trigger		0.1		IV F2
SOS trigger		0.1		IV F2
Ele DT		0.3		IV F3
Coincidence block.		0.1		IV F4
Particle ID		0.2		IV E
Total (Fpi-2)	1.2 (0.9)	1.8–1.9	3.5	V C
Total (Fpi-1)	0.7	1.7–2.0	2.8	V C

into uncertainties that are the same for all t-values at a given ϵ value, and ones that are also uncorrelated in t.

All systematic uncertainties for Fpi-2, with their subdivision, are listed in Table VI. They have been added quadratically to obtain the total systematic uncertainty. For Fpi-1, the values are similar, and only the total systematic uncertainties for the different categories are given. The "instrumental" and model uncertainties have been already discussed in previous sections. The uncertainties in the acceptance are based on extensive single-arm elastic and deep-inelastic measurements (both from the present experiment and from Refs. [38,39]), on ^{1}H($e, e'p$) data, and on how well the sieve slit is reproduced by the used optical matrix elements. The influence of the uncertainties in the offsets in the kinematic variables, such as beam energy, momenta, and angles, was determined by changing the variables by their uncertainty and evaluating the resultant changes in the separated cross sections.

The largest fully correlated systematic uncertainties are the ones due to the radiative corrections, pion absorption, and pion decay, resulting in a total correlated uncertainty of 3–4%. The fully uncorrelated systematic uncertainty is dominated by acceptance, resulting in a total uncorrelated uncertainty of 0.7–1.2%. The largest contributions to the t-correlated uncertainty are acceptance, model dependence,

TABLE VII. Separated cross sections σ_L, σ_T, σ_{LT}, and σ_{TT} for the ^{1}H$(e, e'\pi^+)n$ reaction for Fpi-1 and Fpi-2. The two uncertainties given for σ_L are the combination of statistical and t-uncorrelated systematic uncertainties, and the combination of the ϵ-correlated (scale) and ϵ-uncorrelated, t-correlated uncertainties. This distinction is relevant when extracting values of F_π from the measured values of σ_L (see [12]). The uncertainties for σ_T, σ_{LT}, and σ_{TT} include all uncertainties.

$\overline{Q^2}$ (GeV^2)	$\overline{W}$ (GeV)	$-t$ (GeV^2)	σ_L (μb/GeV^2)	σ_T (μb/GeV^2)	σ_{LT} (μb/GeV^2)	σ_{TT} (μb/GeV^2)
			$Q^2 = 0.60$ GeV^2, $W = 1.95$ GeV			
0.526	1.983	0.026	$31.360 \pm 1.602, 1.927$	8.672 ± 1.241	1.982 ± 0.491	-0.187 ± 0.71
0.576	1.956	0.038	$24.410 \pm 1.119, 1.774$	10.660 ± 1.081	1.581 ± 0.288	-2.034 ± 0.427
0.612	1.942	0.050	$20.240 \pm 1.044, 1.583$	10.520 ± 1.000	0.409 ± 0.255	-3.811 ± 0.406
0.631	1.934	0.062	$14.870 \pm 1.155, 1.366$	10.820 ± 0.992	-0.745 ± 0.302	-5.117 ± 0.524
0.646	1.929	0.074	$11.230 \pm 1.469, 1.210$	10.770 ± 1.097	-1.020 ± 0.390	-6.966 ± 0.816
			$Q^2 = 0.75$ GeV^2, $W = 1.95$ GeV			
0.660	1.992	0.037	$20.600 \pm 1.976, 1.895$	9.812 ± 1.532	0.565 ± 0.393	0.208 ± 0.623
0.707	1.961	0.051	$16.280 \pm 1.509, 1.788$	10.440 ± 1.344	1.135 ± 0.268	-0.454 ± 0.420
0.753	1.943	0.065	$14.990 \pm 1.270, 1.573$	8.580 ± 1.150	0.618 ± 0.206	-1.910 ± 0.378
0.781	1.930	0.079	$11.170 \pm 1.214, 1.416$	9.084 ± 1.091	-0.409 ± 0.197	-2.547 ± 0.419
0.794	1.926	0.093	$9.949 \pm 1.376, 1.277$	8.267 ± 1.110	-0.827 ± 0.220	-3.474 ± 0.534
			$Q^2 = 1.00$ GeV^2, $W = 1.95$ GeV			
0.877	1.999	0.060	$14.280 \pm 1.157, 1.103$	7.084 ± 0.791	1.049 ± 0.294	-0.794 ± 0.474
0.945	1.970	0.080	$11.840 \pm 0.887, 0.978$	6.526 ± 0.657	1.339 ± 0.205	-1.584 ± 0.329
1.010	1.943	0.100	$9.732 \pm 0.773, 0.837$	5.656 ± 0.572	0.719 ± 0.164	-0.582 ± 0.302
1.050	1.926	0.120	$7.116 \pm 0.789, 0.747$	5.926 ± 0.570	0.331 ± 0.158	-1.277 ± 0.360
1.067	1.921	0.140	$4.207 \pm 1.012, 0.612$	5.802 ± 0.656	0.087 ± 0.187	-0.458 ± 0.471
			$Q^2 = 1.60$ GeV^2, $W = 1.95$ GeV			
1.455	2.001	0.135	$5.618 \pm 0.431, 0.442$	3.613 ± 0.294	0.537 ± 0.125	-0.022 ± 0.200
1.532	1.975	0.165	$4.378 \pm 0.356, 0.390$	3.507 ± 0.257	0.356 ± 0.095	-0.268 ± 0.156
1.610	1.944	0.195	$3.191 \pm 0.322, 0.351$	3.528 ± 0.241	0.143 ± 0.081	-0.126 ± 0.153
1.664	1.924	0.225	$2.357 \pm 0.313, 0.310$	3.354 ± 0.228	-0.028 ± 0.076	-0.241 ± 0.167
1.702	1.911	0.255	$2.563 \pm 0.356, 0.268$	2.542 ± 0.227	-0.100 ± 0.085	-0.083 ± 0.196
			$Q^2 = 1.60$ GeV^2, $W = 2.22$ GeV			
1.416	2.274	0.079	$6.060 \pm 0.464, 0.564$	2.802 ± 0.27	0.195 ± 0.073	-0.346 ± 0.177
1.513	2.242	0.112	$4.470 \pm 0.342, 0.457$	2.459 ± 0.21	0.370 ± 0.081	-0.500 ± 0.169
1.593	2.213	0.139	$3.661 \pm 0.303, 0.397$	2.198 ± 0.19	0.334 ± 0.089	-0.481 ± 0.139
1.667	2.187	0.166	$2.975 \pm 0.294, 0.358$	2.124 ± 0.18	0.235 ± 0.081	-0.469 ± 0.139
1.763	2.153	0.215	$1.630 \pm 0.292, 0.315$	2.369 ± 0.19	0.247 ± 0.087	-0.823 ± 0.300
			$Q^2 = 2.45$ GeV^2, $W = 2.22$ GeV			
2.215	2.308	0.145	$2.078 \pm 0.180, 0.229$	1.635 ± 0.11	0.217 ± 0.034	-0.060 ± 0.163
2.279	2.264	0.202	$1.365 \pm 0.125, 0.179$	1.395 ± 0.08	0.168 ± 0.025	-0.199 ± 0.066
2.411	2.223	0.245	$0.980 \pm 0.110, 0.159$	1.337 ± 0.08	0.159 ± 0.023	-0.163 ± 0.045
2.539	2.181	0.288	$0.786 \pm 0.114, 0.150$	1.304 ± 0.08	0.128 ± 0.018	-0.187 ± 0.120
2.703	2.127	0.365	$0.564 \pm 0.123, 0.137$	1.240 ± 0.08	0.161 ± 0.020	-0.234 ± 0.109

and kinematic offsets, resulting in a total ϵ-uncorrelated, t-correlated uncertainty of 1.7–2.0%. As mentioned, these ϵ-uncorrelated uncertainties are multiplied by about a factor of 3 when performing the L/T separation. As a result, they are the dominating systematic uncertainty for, e.g., σ_L.

VI. CROSS SECTION RESULTS

The separated cross sections are listed in Table VII and shown in Figs. 17 (σ_L, σ_T) and 18 (σ_{LT}, σ_{TT}). In the following subsections, the global dependences of σ_L and σ_T will be

reviewed, and the data compared with model calculations for the ^{1}H$(e, e'\pi^+)n$ reaction.

A. Global dependences of the separated cross sections

At all values of Q^2, the longitudinal cross section σ_L shows the characteristic falloff with $-t$ due to the pion pole. Its magnitude (at constant W) drops with increasing Q^2, mainly because the value of $-t_{\min}$ increases with Q^2. The transverse cross section σ_T is largely flat with $-t$, while its magnitude drops with increasing Q^2. The interference term σ_{LT} is rather
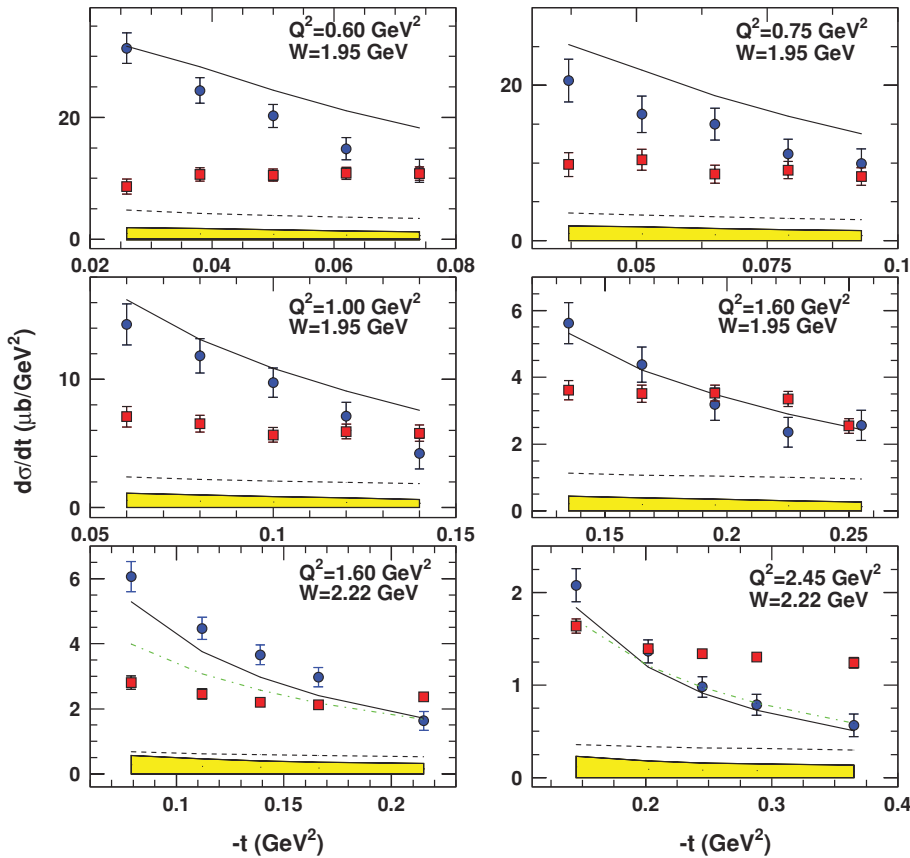
FIG. 17. (Color online) Separated cross sections, σ_L (circles) and σ_T (squares) at central values of $Q^2 = 0.60, 0.75, 1.00, 1.60$ GeV^2 ($W = 1.95$ GeV), and $Q^2 = 1.60, 2.45$ GeV^2 ($W = 2.22$ GeV). The values of $\overline{W}$ and $\overline{Q^2}$ are different for each $-t$ bin. The error bars for σ_L indicate the statistical and uncorrelated systematic uncertainties in both ϵ and $-t$ combined in quadrature. The error band denotes the correlated part of the systematic uncertainty by which all data points move collectively for σ_L. The error bars for σ_T represent the total uncertainty. The curves denote Regge calculations (VGL, [48,49]) for σ_L (solid line) and σ_T (dashed line) for $\Lambda_\pi^2 = 0.462$ GeV^2 and $\Lambda_\rho^2 = 1.5$ GeV^2. Also shown is a calculation for σ_L (dashed-dotted line) using a generalized parton distribution (GPD) model [50] including power corrections.
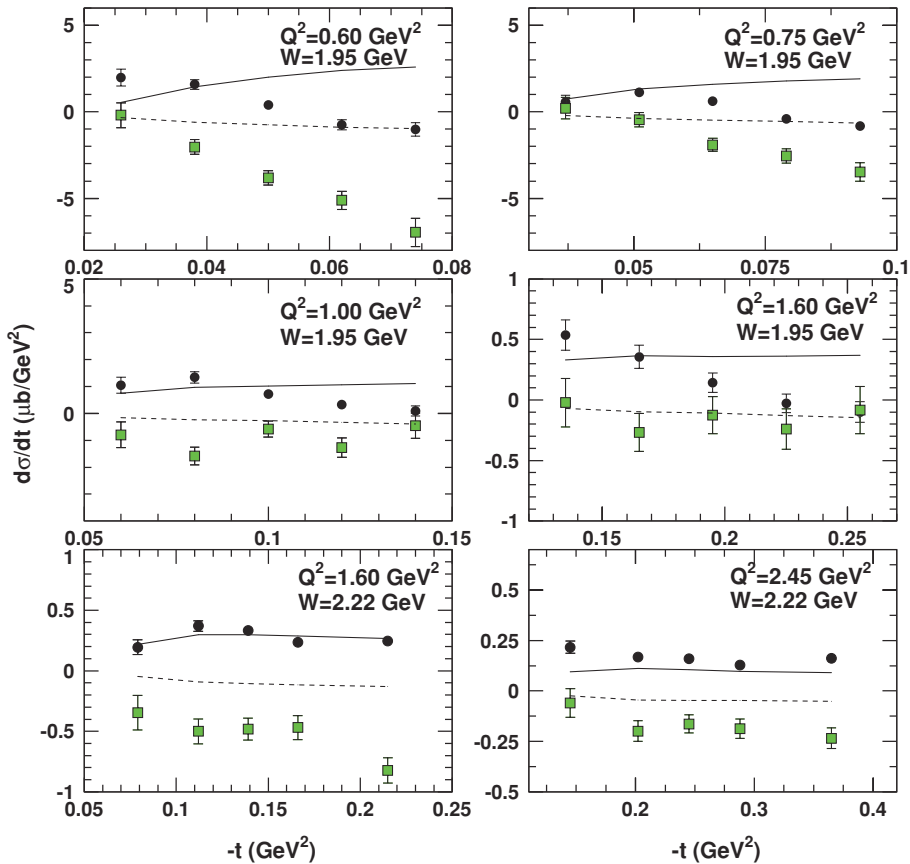
FIG. 18. (Color online) Interference terms, σ_{LT} (circles) and σ_{TT} (squares) at central values of $Q^2 = 0.60, 0.75, 1.00, 1.60$ GeV^2 ($W = 1.95$ GeV), and $Q^2 = 1.60, 2.45$ GeV^2 ($W = 2.22$ GeV). The curves denote Regge calculations (VGL [48,49]) for σ_{LT} (solid line) and σ_{TT} (dashed line) with $\Lambda_\pi^2 = 0.462$ GeV^2 and $\Lambda_\rho^2 = 1.5$ GeV^2.

small, while the value of σ_{TT}, which clearly shows the behavior of going to 0 at $t_{\min}$, drops rapidly with increasing Q^2.

With the availability of our precision separated cross sections over an extended kinematic range, it is interesting to look into the global dependences of the longitudinal and transverse cross sections upon W, Q^2, and t. A similar study was done in Ref. [8] with the more limited data then available. For the purpose of this study, both our cross sections and those of Refs. [6,8] were used. For σ_T, the photoproduction data of Ref. [51] were also used.

The W dependences of the earlier σ_L and σ_T data were observed [8] to follow $(W^2 - M^2)^{-2}$, where M is the nucleon mass. Our $Q^2 = 1.60$ GeV^2 data at $W = 1.95, 2.22$ GeV are consistent with this within about 10%.

Because σ_L is dominated by the pion-pole contribution, its Q^2 dependence is largely given by $Q^2 F_\pi^2(Q^2)$. Figure 19 shows the results for σ_L, where all cross sections have been scaled to $W = 2.19$ GeV according to $(W^2 - M^2)^{-2}$, and to $Q^2 = 0.70$ GeV^2 using the factor $Q^2 F_\pi^2(Q^2)$, where F_π was assumed to follow the monopole form $(1 + \frac{Q^2}{m_\rho^2})^{-1}$. Although overall the σ_L data follow an almost exponential t dependence, upon close inspection it is observed that at constant Q^2 the data deviate from that curve; i.e., the Q^2 and t dependences do not factorize completely, and at both high and low $-t$, deviations from a pure exponential are observed. Fitting the data with an exponential $Be^{-b|t|}$ results in a slope parameter $b = 10.5 \pm 1.8$ GeV^{-2}, and a normalization factor $B = 19.0 \pm 2.0$. Such a form describes all σ_L data within about 50%.

No simple prediction exists for the Q^2 dependence of σ_T. Figure 20 shows the Q^2 dependence of the σ_T data at $-t = 0.08$ and 0.2 GeV^2, scaled to $W = 2.19$ GeV. The data show
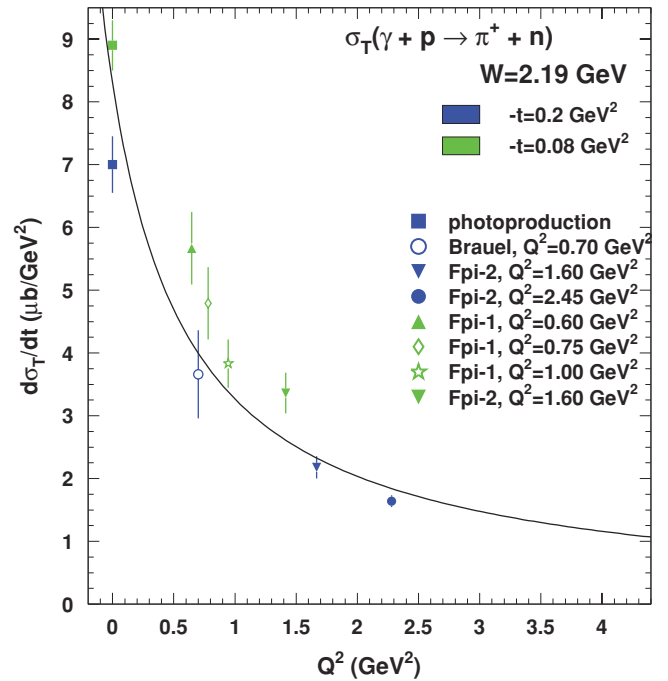

FIG. 20. (Color online) Q^2 dependence of the transverse π^+ cross section at $-t = 0.08$ and 0.2 GeV^2. The cross sections are scaled to $W = 2.19$ GeV. The photoproduction point is from Ref. [51]. The curve indicates a parametrization for σ_T of the form $\frac{C}{1+DQ^2}$.

a clear dependence on Q^2, which is reasonably well described by a factor of the form $\frac{C}{1+DQ^2}$.

Figure 21 displays the electroproduction and photoproduction σ_T data scaled to $W = 2.19$ GeV using the functional form
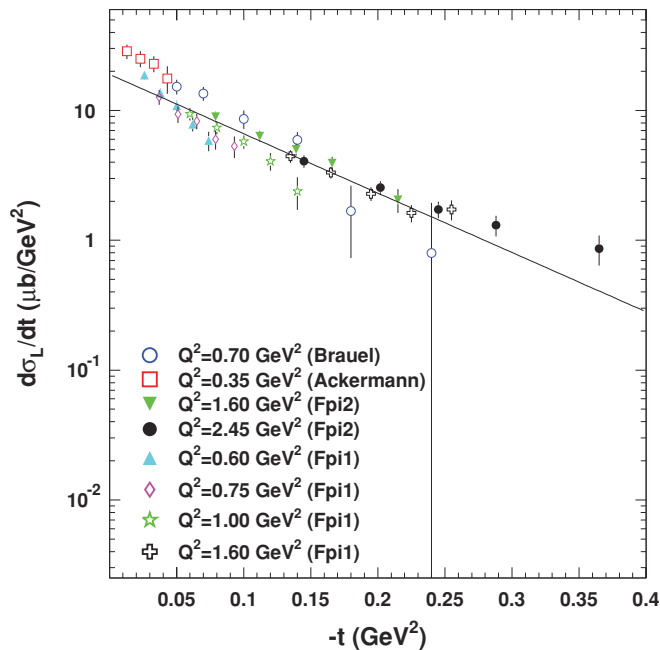

FIG. 19. (Color online) t dependence of the longitudinal π^+ cross section. The data from Refs. [6,8,10,11] are scaled in W and Q^2 (see the text) to common values of $W = 2.19$ GeV and $Q^2 = 0.7$ GeV^2.
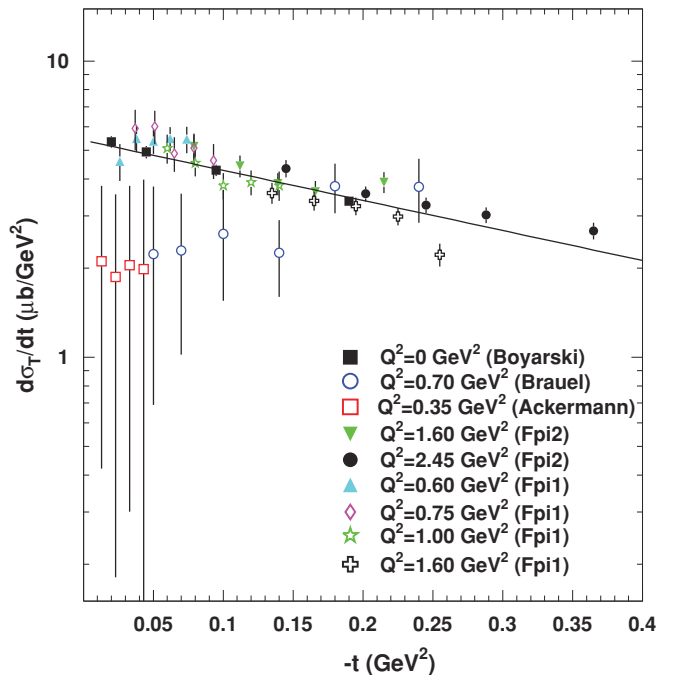

FIG. 21. (Color online) t dependence of the transverse π^+ cross section. The data from Refs. [6,8,10,11,51] are scaled to common values of $W = 2.19$ GeV and $Q^2 = 0.7$ GeV^2 (see text).
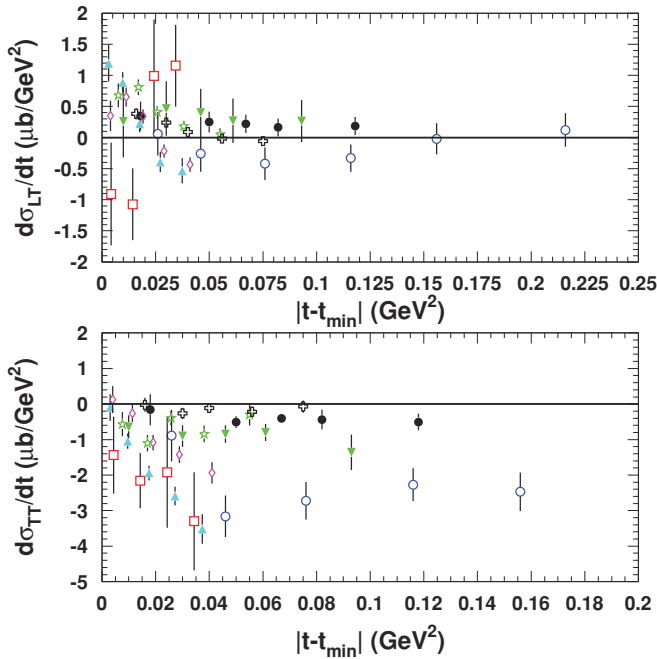
FIG. 22. (Color online) $t - t_{\min}$ dependence of the interference terms. Both are scaled to common values of $W = 2.19$ GeV and $Q^2 = 0.70$ GeV^2, see the text. The plotting symbols are the same as in Fig. 21.

$(W^2 - M^2)^{-2}$, and to $Q^2 = 0.7$ GeV^2 according to $\frac{C}{1+DQ^2}$, where $C = 8.21 \pm 1.7$ and $D = 1.54 \pm 1.7$. An exponential in t analogous to the form used for $\sigma_{\rm L}$ describes the photoproduction and electroproduction data from Fpi-1 and Fpi-2 to within 30%, while the DESY data are overpredicted by a factor of about 2. An exponential fit results in a slope parameter of $b = 2.3 \pm 1.5$ GeV^{-2}, and a normalization factor of $B = 5.4 \pm 1.4$. Though the slope is less steep than for $\sigma_{\rm L}$, it is clear that $\sigma_{\rm T}$ is not independent of t and Q^2 in these kinematics. This is different from the conclusions of Ref. [8].

Figure 22 shows the $t - t_{\min}$ dependence of $\sigma_{\rm LT}$ and $\sigma_{\rm TT}$. The $\sigma_{\rm LT}$ data are scaled to common values of $W = 2.19$ GeV and $Q^2 = 0.70$ GeV^2 using a factor $Q^2 F_\pi$. The $\sigma_{\rm TT}$ data were scaled in Q^2 analogous to $\sigma_{\rm T}$. In both cases, no overall trend could be identified because of the large scatter of the data.

B. VGL Regge Model

In Refs. [48,49], Vanderhaeghen, Guidal, and Laget (VGL) developed a Regge model for pion production, in which the pole-like propagators of Born term models are replaced with Regge propagators; i.e., the interaction is effectively described by the exchange of a family of particles with the same quantum numbers instead of a single particle. For forward pion production, the dominant exchanges are the π and ρ trajectories. These determine the t dependence of the cross section without the use of a $g_{\pi NN}(t)$ factor. Since the t-channel π diagram is by itself not gauge invariant, in the VGL model the s-channel (for π^+ production) or u-channel (for π^- production) nucleon exchange diagram was also Reggeized, to ensure gauge invariance of their sum. The model is parameter

free, as the coupling constants at the vertices (such as $g_{\rho\pi\gamma}$) are well determined by precise studies and analyses in the resonance region.

The VGL model was first applied to pion photoproduction [48]. The model gave a good and consistent description of the W and t dependences of the available π^+ and π^- photoproduction data including the spin asymmetries. The fact that both the π (unnatural-parity) and the ρ (natural-parity) trajectories are incorporated in the model proved to be essential to explain the different behaviors of π^+ and π^- photoproduction.

In Refs. [48,49], the model was extended to pion electroproduction. As the π- and ρ-exchange amplitudes are separately gauge invariant, two different electromagnetic form factors were introduced for the π and ρ exchanges without violating the gauge invariance of the model. In both cases, monopole forms are used. Form factors of monopole type were taken for the π and ρ exchanges:

$$F_{\pi,\rho}(Q^2) = [1 + Q^2/\Lambda_{\pi,\rho}^2]^{-1}. \tag{17}$$

The model gave a good description of π^+ electroproduction data out to large values of $-t$ at W values of 2.15 and 3.1 GeV for $Q^2 = 1.2$ GeV^2 [4], and of the π^-/π^+ ratio at $W = 2.19$ GeV, $Q^2 = 0.7$ and 1.35 GeV^2 [8].

The VGL model is compared with our electroproduction data in Figs. 17 and 18. The VGL cross sections were evaluated at the same $\overline{W}$ and $\overline{Q}^2$ values as the data. Over the range of $-t$ covered by this work, $\sigma_{\rm L}$ is completely determined by the π trajectory, while $\sigma_{\rm T}$, $\sigma_{\rm TT}$, and $\sigma_{\rm LT}$ are also sensitive to the ρ exchange contribution. Comparison of the model calculations against previous data gave a value for Λ_π^2 of about 0.45–0.50 GeV^2. Here, calculations with a common value of $\Lambda_\pi^2 = 0.462$ GeV^2 are shown. This is the same value as that used in Refs. [48,49]. The value of Λ_ρ^2 is more poorly known. Here, calculations with $\Lambda_\rho^2 = 1.500$ GeV^2 are shown, where this upper value is determined from the application of the VGL model to kaon electroproduction [52].

With a single value of $\Lambda_\pi^2 = 0.462$ GeV^2, the VGL model does an overall good job of describing the magnitude, and t, W and Q^2 dependences of our $\sigma_{\rm L}$ data. However, as shown in Fig. 17, the description of the t dependence is not as good for $Q^2 \leqslant 1.00$ GeV^2, $W = 1.95$ GeV, where the model prediction is too flat in comparison to the experimental data. The model also strongly underestimates $\sigma_{\rm T}$, almost independent of the value of Λ_ρ^2, and this underestimation appears to grow with Q^2, the falloff of the data with Q^2 being less than that of the model. This deficiency is also reflected in a too-small prediction for $\sigma_{\rm TT}$. Please note that VGL definition of $\sigma_{\rm TT}$ differs from ours by a minus sign, which has been included here. The $\sigma_{\rm LT}$ calculations at $W = 2.22$ GeV are generally satisfactory, but the agreement with the data is much worse at the lower value $W = 1.95$ GeV, the data getting smaller or even becoming negative at larger values of $-t$.

Recently, the VGL model was extended [53] by including, apart from a slightly different way to handle the gauge invariance, a hard scattering between the virtual photon and a quark, followed by hadronization of the system into a pion
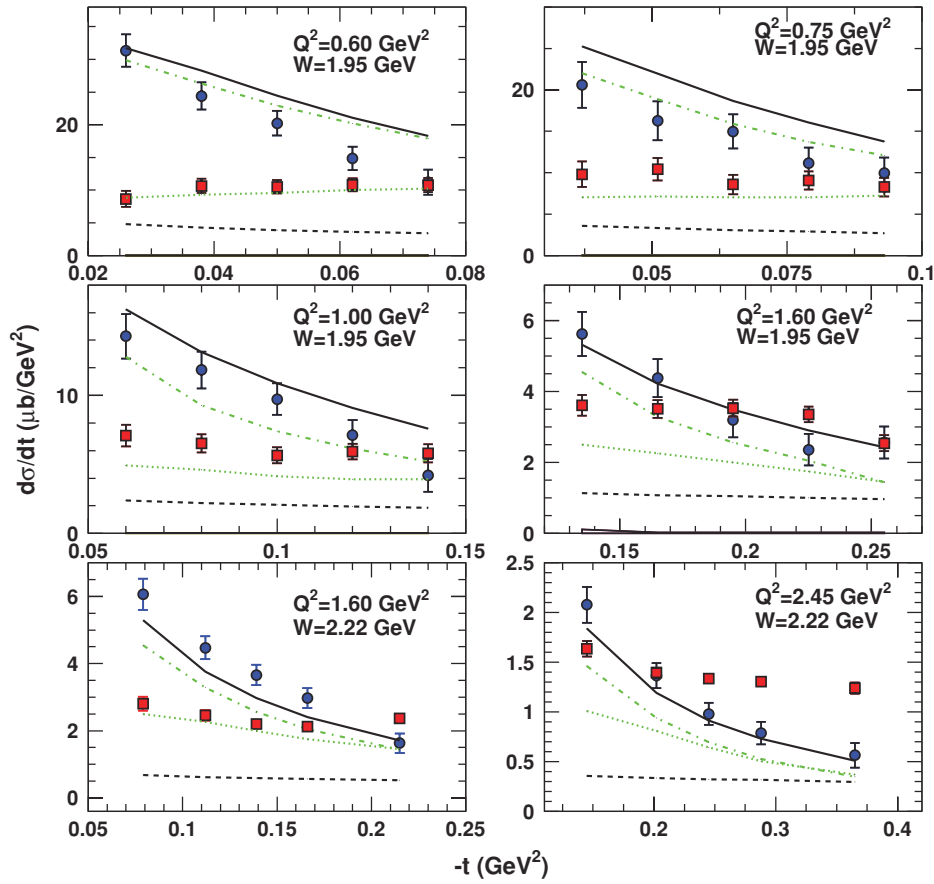
FIG. 23. (Color online) Separated π^+ electroproduction cross sections, σ_L (circles) and σ_T (squares) at central values of $Q^2 = 0.60, 0.75, 1.00, 1.60$ GeV^2 ($W = 1.95$ GeV), and $Q^2 = 1.60, 2.45$ GeV^2 ($W = 2.22$ GeV) compared with the predictions of the VGL Regge [48,49] (solid and dotted line) and FGLO effective Lagrangian [54,55] (dot-dashed and dashed line) models. A common value of $\Lambda_\pi^2 = 0.462$ GeV^2 is used. Note that the average values of W and Q^2 are different for each $-t$ bin. The error bars denote statistical and t-uncorrelated systematic uncertainties combined in quadrature. In addition, there is a t- and ϵ-correlated systematic uncertainty of 4–6%, by which all data points move collectively.

plus residual nucleon. With plausible assumptions, a good description of σ_T was obtained, with no influence on σ_L.

C. FGLO effective Lagrangian model

A more recent development is the effective Lagrangian model of Faessler, Gutsche, Lyubovitskij, and Obukhovsky (FGLO [54,55]). This is a modified Born term model, in which an effective Lagrangian is used to describe nucleon, pion, ρ, and photon degrees of freedom. The (combined) effect of s- and u-channel contributions, which interferes with the pion t pole, is modeled using a constituent quark model. The authors pay special attention to the role of the ρ meson in π^+ electroproduction and show that the ρt-pole contribution is very important for obtaining a good description of the magnitude of σ_T. When comparing vector and tensor representations of the ρ contribution, the latter was found to give better results. Unlike the VGL model, the σ_L cross section depends here also on the ρ exchange, because of the interference of the π and tensor ρ exchange contributions. The model contains a few free parameters, such as the renormalization constant of the Kroll-Ruderman contact term used to model the $s(u)$ channel, and t-dependent strong meson-nucleon vertices, which are parametrized in monopole form, as are the electromagnetic form factors. The corresponding parameters were adjusted to give overall good agreement with our σ_L and σ_T data.

The FGLO model calculation is compared with our data in Fig. 23. A common value of $\Lambda_\pi^2 = 0.462$ GeV^2 is used throughout. The other model parameters were fixed at the values assigned by the authors. Generally, the agreement of the FGLO model with the σ_L data is rather good, but the model gives a too-flat t dependence at $Q^2 = 0.60$ GeV^2, $W = 1.95$ GeV. While on average the model calculation is in agreement with the σ_T data, it fails to describe the Q^2 and W dependences. For example, the model underpredicts the $Q^2 = 1.60$ GeV^2, $W = 1.95$ GeV σ_T data by about a factor of 2, while those at $Q^2 = 1.60$ GeV^2, $W = 2.22$ GeV are reproduced, and the $Q^2 = 2.45$ GeV^2, $W = 2.22$ GeV σ_T data underpredicted again by 20–60%. No calculations are available for the interference cross sections.

D. VGG GPD model

Vanderhaeghen, Guichon, and Guidal (VGG) [50] have performed a calculation for σ_L using generalized parton distributions (GPDs). This approach is based on a soft-hard factorization theorem [56].

Since the one-gluon perturbative diagram severely underestimates the value of the pion form factor at the relevant Q^2, power corrections due to intrinsic transverse momenta and soft overlap contributions were included in the calculation, thereby increasing the calculated cross sections by an order of magnitude. The VGG GPD model is compared to our

electroproduction data in Fig. 17. The GPD calculation gives a rather good description of the t dependence of the $W >$ 2 GeV data, while the Q^2 dependence is also described fairly well. The determination of the onset of this regime remains one of the great challenges in contemporary GPD studies [57]. Measurements to address this issue, approved for data taking after the completion of the JLab upgrade [58], may be expected to place a constraint on the value of Q^2 for which one can reliably apply perturbative QCD concepts and extract GPDs.

VII. SUMMARY AND CONCLUSIONS

Precision data for the $^1\mathrm{H}(e, e'\pi^+)n$ reaction were obtained to study the pion form factor in the regime $Q^2 =$ 0.5–3.0 GeV^2. The data were acquired at JLab making use of the high-intensity, continuous CEBAF electron beams and the magnetic spectrometers in Hall C.

The $^1\mathrm{H}(e, e'\pi^+)n$ cross sections were measured for values of the Mandelstam variable t close to its minimum value $t_{\min}$ for (central) four-momentum transfers ranging from $Q^2 = 0.60$ to 2.45 GeV^2, at an invariant mass of the photon-nucleon system of $W = 1.95$ or 2.22 GeV. Since F_π is to be determined from the longitudinal part, σ_L, of the cross section, the measured cross sections were decomposed into the four structure functions σ_L, σ_T, σ_{LT}, and σ_{TT} at every Q^2. This required measuring the cross section at two values of the virtual photon polarization ϵ and as function of the azimuthal angle ϕ of the produced pion. In the analysis, a Monte Carlo simulation of the whole experimental setup was used. The simulation included a model cross section fitted to the data and thus allowed for accurate acceptance corrections.

Good control of the systematic uncertainty is extremely important in L/T separations, as the error bars are inflated by $\Delta\epsilon$. Therefore, all parts of the experimental setup and the analysis procedures were carefully inspected and calibrated. This included the optical properties of the spectrometers, the tracking and particle identification methods, and the various efficiencies. As a result, the total systematic uncertainty of the unseparated cross sections could be reduced to a point-to-point uncertainty below 2%, plus a scale uncertainty of

less than 3.5%. The final separated cross sections have a total uncertainty (statistical plus systematic) between 8% and 15%.

The longitudinal cross section σ_L shows the characteristic falloff with $-t$ due to the pion pole and largely behaves as a function of Q^2 according to $Q^2 F_\pi(Q^2)^2$. The transverse cross section σ_T depends only a little on t, but our results indicate a clear dependence on Q^2, which, including photoproduction data, can be described as $\frac{1}{1+bQ^2}$. This is different from what was concluded from earlier electroproduction results at DESY. The interference term σ_{LT} is rather small, while the value of σ_{TT} drops fast with increasing Q^2.

The separated cross sections were compared with the results of model calculations for the $^1\mathrm{H}(e, e'\pi^+)n$ reaction, which use Regge trajectories, effective Lagrangians, or generalized parton distributions. They all provide a fair to good description of the longitudinal cross section. The description of the transverse cross section is much worse, however. The Regge model strongly underpredicts σ_T, while the Lagrangian model yields good agreement at some values of W and Q^2, but fails when either W or Q^2 is varied. Clearly, more theoretical work has to be done to understand the behavior of σ_T (and also of the interference structure functions σ_{LT} and σ_{TT}) of the $^1\mathrm{H}(e, e'\pi^+)n$ reaction as a function of W, Q^2, and t.

[1] G. T. Adylov *et al.*, Phys. Lett. **B51**, 402 (1974); Nucl. Phys. **B128**, 461 (1977).

[2] E. B. Dally *et al.*, Phys. Rev. Lett. **48**, 375 (1982); Phys. Rev. Lett. **39**, 1176 (1977); Phys. Rev. D **24**, 1718 (1981).

[3] S. R. Amendolia *et al.*, Nucl. Phys. **B277**, 168 (1986); Phys. Lett. **B138**, 454 (1984).

[4] C. J. Bebek *et al.*, Phys. Rev. D **13**, 25 (1976).

[5] C. J. Bebek *et al.*, Phys. Rev. D **17**, 1693 (1978).

[6] H. Ackermann *et al.*, Nucl. Phys. **B137**, 294 (1978).

[7] P. Brauel *et al.*, Phys. Lett. **B69**, 253 (1977); Z. Phys. C **3**, 101 (1979).

[8] P. Brauel *et al.*, Phys. Lett. **B65**, 184 (1976).

[9] J. Volmer *et al.*, Phys. Rev. Lett. **86**, 1713 (2001).

[10] V. Tadevosyan *et al.*, Phys. Rev. C **75**, 055205 (2007).

[11] T. Horn *et al.*, Phys. Rev. Lett. **97**, 192001 (2006).

[12] G. M. Huber *et al.*, Phys. Rev. C **78**, 045203 (2008).

[13] T. de Forest, Jr., Ann. Phys. (NY) **45**, 365 (1967); J. D. Sullivan, Phys. Lett. **B33**, 179 (1970).

[14] A. S. Raskin and T. W. Donnelly, Ann. Phys. (NY) **191**, 78 (01989); M. Diehl and S. Sapeta, Eur. Phys. J. C **41**, 515 (2005).

[15] D. J. Mack, H. Blok, and G. Huber, TJNAF Proposal 93-021, 1993.

[16] G. Huber, H. Blok, and D. J. Mack, TJNAF Proposal 01-004, 2001.

[17] CEBAF Conceptual Design report, Basic Experimental Equipment, SURA, April 1990.

[18] C. W. Leemann, D. R. Douglas, and G. A. Krafft, Annu. Rev. Nucl. Part. Sci. **51**, 413 (2001).

[19] K. Unser, AIP Conf. Proc. **252**, 266 (1992).

[20] G. Niculescu, Ph.D. thesis, Hampton University, 1998.

[21] C. Yan *et al.*, Nucl. Instrum. Methods Phys. Res. A **365**, 46 (1995).

[22] C. Yan *et al.*, CEBAF-PR-93-004, 1993.

[23] J. Dunne, Cryo and Dummy Target Information, TJNAF Hall C document, 1998.

[24] D. G. Meekins, Ph.D. thesis, College of William & Mary, 1998.

[25] B. Terburg, Ph.D. thesis, University of Illinois, 1998.

[26] J. R. Arrington, Ph.D. thesis, California Institute of Technology, 1998.

[27] J. Volmer, Ph.D. thesis, Vrije Universiteit, Amsterdam, 2000.

[28] D. Gaskell, Ph.D. thesis, Oregon State University, 2001.

[29] V. E. Hart *et al.*, in *Proceedings of the 1992 Linac Conference Ottawa, Canada,* edited by C. R. Hoffmann (Chalk River Laboratories Report No. AECL-10728, 1992), p. 737.

[30] D. van Westrum, Ph.D. thesis, University of Colorado, Boulder, 1999.

[31] O. K. Baker *et al.*, Nucl. Instrum. Methods Phys. Res. A **367**, 92 (1995).

[32] R. Asaturyan *et al.*, Nucl. Instrum. Methods Phys. Res. A **548**, 364 (2005).

[33] R. M. Mohring, Ph.D. thesis, University of Maryland, 1999.

[34] T. Horn, Ph.D. thesis, University of Maryland, 2006.

[35] D. J. Abbott *et al.*, in Proceedings of the 1995 IEEE Conference on Real-Time Computer Applications in Nuclear, Particle and Plasma Physics, May 1995, p. 147.

[36] C. Xu *et al.*, SOS Optics Calibrations, http://www.jlab.org/xu/OPTCHECK.html.

[37] B. Clasie, Ph.D. thesis, Massachussetts Institute of Technology, 2004.

[38] M. E. Christy *et al.*, Phys. Rev. C **70**, 015206 (2004).

[39] V. Tvaskis, Ph.D. thesis, Vrije Universiteit te Amsterdam, 2004.

[40] T. Horn *et al.*, JLab-TN07-067, 2007.

[41] K. Makino and M. Berz, Nucl. Instrum. Methods Phys. Res. A **427**, 338 (1999).

[42] L. M. Mo and Y. S. Tsai, Rev. Mod. Phys. **41**, 205 (1969).

[43] R. Ent, B. W. Filippone, N. C. R. Makins, R. G. Milner, T. G. ONeill, and D. A. Wasson, Phys. Rev. C **64**, 054610 (2001).

[44] W. Melnitchouk (private communication).

[45] N. Makins, Ph.D. thesis, Massachusetts Institute of Technology, 1994.

[46] P. E. Bosted, Phys. Rev. C **51**, 409 (1995).

[47] J. R. Arrington, Phys. Rev. C **69**, 022201(R) (2004).

[48] M. Vanderhaeghen, M. Guidal, and J.-M. Laget, Phys. Rev. C **57**, 1454 (1998).

[49] M. Vanderhaeghen, M. Guidal, and J.-M. Laget, Nucl. Phys. **A627**, 645 (1997).

[50] M. Vanderhaeghen, P. A. M. Guichon, and M. Guidal, Phys. Rev. Lett. **80**, 5064 (1998); Phys. Rev. D **60**, 094017 (1999).

[51] A. Boyarski, Phys. Rev. Lett. **20**, 300 (1968).

[52] M. Guidal, J.-M. Laget, and M. Vanderhaeghen, Phys. Rev. C **61**, 025204 (2000).

[53] M. M. Kaskulov, K. Gallmeister, and U. Mosel, arXiv:0804.1834v2 [hep-ph].

[54] I. T. Obukhovsky, D. Fedorov, A. Faessler, T. Gutsche, and V. E. Lyubovitsky, Phys. Lett. **B634**, 220 (2006).

[55] A. Faessler, T. Gutsche, V. E. Lyubovitskij, and I. T. Obukhovsky, Phys. Rev. C **76**, 025213 (2007).

[56] J. C. Collins, L. Frankfurt, and M. Strikman, Phys. Rev. D **56**, 2982 (1997).

[57] T. Horn *et al.*, arXiv:0707.1794 (2007).

[58] T. Horn, G. Huber *et al.*, Approved Jefferson Lab experiment E12-07-103, http://www.jlab.org/exp_prog/proposals/07/PR12-07-103.pdf.